Monthly Notices of the ROYAL ASTRONOMICAL SOCIETY

MNRAS **510,** 5376–5391 (2022) https://doi.org/10.1093/mnras/stab3793
Advance Access publication 2022 January 4

Exploiting non-linear scales in galaxy–galaxy lensing and galaxy clustering: A forecast for the dark energy survey

Andrés N. Salcedo [1]★ David H. Weinberg,[1,2] Hao-Yi Wu [3] and Benjamin D. Wibking [4]

[1]*Department of Astronomy and Center for Cosmology and AstroParticle Physics, The Ohio State University, Columbus OH 43210, USA*
[2]*Institute for Advanced Study, Princeton NJ 08540, USA*
[3]*Department of Physics, Boise State University, Boise ID 83725, USA*
[4]*Mount Stromlo Observatory, Australian National University, Cotter Road, Weston Creek ACT 2611, Australia*

Accepted 2021 December 24. Received 2021 December 24; in original form 2021 July 15

ABSTRACT

The combination of galaxy–galaxy lensing (GGL) and galaxy clustering is a powerful probe of low-redshift matter clustering, especially if it is extended to the non-linear regime. To this end, we use an *N*-body and halo occupation distribution (HOD) emulator method to model the redMaGiC sample of colour-selected passive galaxies in the Dark Energy Survey (DES), adding parameters that describe central galaxy incompleteness, galaxy assembly bias, and a scale-independent multiplicative lensing bias $A_{\rm lens}$. We use this emulator to forecast cosmological constraints attainable from the GGL surface density profile $\Delta\Sigma(r_p)$ and the projected galaxy correlation function $w_{p,\,gg}(r_p)$ in the final (Year 6) DES data set over scales $r_p = 0.3$–$30.0\,h^{-1}$ Mpc. For a 3 per cent prior on $A_{\rm lens}$ we forecast precisions of 1.9 per cent, 2.0 per cent, and 1.9 per cent on Ω_m, σ_8, and $S_8 \equiv \sigma_8\Omega_m^{0.5}$, marginalized over all halo occupation distribution (HOD) parameters as well as $A_{\rm lens}$. Adding scales $r_p = 0.3$–$3.0\,h^{-1}$ Mpc improves the S_8 precision by a factor of $\sim$1.6 relative to a large scale (3.0–$30.0\,h^{-1}$ Mpc) analysis, equivalent to increasing the survey area by a factor of $\sim$2.6. Sharpening the $A_{\rm lens}$ prior to 1 per cent further improves the S_8 precision to 1.1 per cent, and it amplifies the gain from including non-linear scales. Our emulator achieves per cent-level accuracy similar to the projected DES statistical uncertainties, demonstrating the feasibility of a fully non-linear analysis. Obtaining precise parameter constraints from multiple galaxy types and from measurements that span linear and non-linear clustering offers many opportunities for internal cross-checks, which can diagnose systematics and demonstrate the robustness of cosmological results.

Key words: methods: numerical – cosmology: theory – dark matter – large-scale structure of Universe.

1 INTRODUCTION

Understanding the origin of cosmic acceleration remains the most pressing challenge of contemporary cosmology. Ambitious cosmological surveys are using a variety of observational probes to measure the histories of cosmic expansion and the growth of matter clustering with high precision over a wide span of redshift (for reviews see e.g. Frieman, Turner & Huterer 2008; Weinberg et al. 2013). Comparing expansion history and structure growth is critical to testing whether cosmic acceleration reflects a breakdown of general relativity (GR) on cosmological scales or a form of dark energy that exerts repulsive gravity within GR. With present data sets, the most powerful constraints on low-redshift matter clustering come from large area weak lensing surveys, which can measure matter clustering directly through cosmic shear or by combining galaxy–galaxy lensing (GGL) with galaxy clustering.

This paper presents methodology for and forecasts of the precision obtainable with the combination of GGL and galaxy clustering in the final data sets from the Dark Energy Survey (DES; The Dark Energy Survey Collaboration 2005; DES Collaboration 2021), building on the work of Wibking et al. (2019, 2020). GGL measures correlations between foreground lens galaxies and a shear map of background source galaxies to infer the lens galaxies' mean excess surface density profile $\Delta\Sigma(r_p)$, which is proportional to the product of the matter density parameter Ω_m and the galaxy-matter cross-correlation function ξ_{gm}. On scales large enough to be described by linear perturbation theory one expects $\xi_{gm} = b_g\xi_{mm}$ and $\xi_{gg} = b_g^2\xi_{mm}$, where b_g is the galaxy bias factor and ξ_{gg} and ξ_{mm} are the galaxy and matter autocorrelation functions, respectively. One can therefore combine GGL and ξ_{gg} to cancel the unknown b_g and constrain $\Omega_m\sqrt{\xi_{mm}} \propto \Omega_m\sigma_8$, where σ_8, the RMS linear theory matter overdensity fluctuation in spheres of radius $8.0\,h^{-1}$ Mpc at $z = 0$, is an overall scaling of the amplitude of matter fluctuations. In practice the best constrained parameter combination is closer to $S_8 \equiv \sigma_8\Omega_m^{0.5}$.

Interpreting GGL and clustering measurements on smaller scales requires a model for the relation between galaxies and dark matter in the non-linear regime, such as the halo occupation distribution (HOD; Jing, Mo & Börner 1998; Peacock & Smith 2000; Scoccimarro et al. 2001; Berlind & Weinberg 2002) or sub-halo abundance matching (Conroy, Wechsler & Kravtsov 2006; Vale & Ostriker 2006). Although these models require additional free parameters, non-linear clustering data can constrain them, so extending to the non-linear regime of GGL and ξ_{gg} can potentially achieve much tighter constraints on cosmological parameters (Yoo et al. 2006; Zheng & Weinberg 2007; Cacciato et al. 2009, 2012, 2013; Leau-

★ E-mail: salcedo.11@osu.edu

thaud et al. 2011; Yoo & Seljak 2012; More et al. 2013). The stakes of this effort are illustrated by a number of recent studies finding that the amplitude of matter clustering inferred from GGL + galaxy clustering is 5–10 per cent lower than the amplitude predicted by extrapolating CMB anisotropies forward to low redshift assuming a ΛCDM cosmological model (Mandelbaum et al. 2013; More et al. 2015; Leauthaud et al. 2017; Joudaki et al. 2018; Singh et al. 2020; Wibking et al. 2020; Krolewski, Ferraro & White 2021).[1] The conflict is strongest on non-linear scales, where the measurement precision is highest but the demands on the accuracy of non-linear modelling are the most stringent (Leauthaud et al. 2017; Lange et al. 2019, 2021). Many cosmic shear studies also find clustering amplitudes lower than the CMB-based prediction, but the discrepancy is less statistically significant (Jee et al. 2016; Hildebrandt et al. 2017; Hikage et al. 2019; Amon et al. 2021; Secco et al. 2021). The recent '3x2pt' analysis of the Year 3 (Y3) DES data, which combines cosmic shear, GGL, and galaxy clustering on scales adequately described by linear theory, yields results compatible with CMB-based ΛCDM predictions, but also compatible with the lower amplitudes reported in the studies listed above (DES Collaboration 2021).

In this study we adopt the HOD framework to model non-linear galaxy bias. HOD methods statistically specify the relationship between galaxies and their host haloes, primarily as a function of host halo mass. In a cosmological context the most important question is whether or not a given HOD parametrization is flexible enough to model the non-linear galaxy bias without producing biased cosmological constraints. One of the most important sources of systematic uncertainty in the galaxy–halo connection is the potential presence of galaxy assembly bias. Galaxy assembly bias refers to the potential for the galaxy occupation inside haloes of the same mass to vary with respect to a secondary halo property. In combination with *halo* assembly bias (e.g. Sheth & Tormen 2004; Gao, Springel & White 2005; Harker et al. 2006; Wechsler et al. 2006; Gao & White 2007; Jing, Suto & Mo 2007; Wang, Mo & Jing 2007; Li, Mo & Gao 2008; Faltenbacher & White 2010; Mao, Zentner & Wechsler 2018; Salcedo et al. 2018; Xu & Zheng 2018; Johnson et al. 2019; Sato-Polito et al. 2019; Mansfield & Kravtsov 2020; Tucci et al. 2021), the potential for halo clustering at fixed mass to vary with respect to a secondary halo property, this can modify the large-scale galaxy clustering making predictions from a standard HOD model inaccurate (Croton, Gao & White 2007; Zu et al. 2008; McCarthy, Zheng & Guo 2019). To provide our HOD framework the flexibility to describe potential galaxy assembly bias we adopt the modifications of Salcedo et al. (2020a; see also McEwen & Weinberg 2018; Wibking et al. 2019; Salcedo et al. 2020b; Xu, Zehavi & Contreras 2021). For our forecasts, we focus on the DES redMaGiC galaxy sample (Rozo et al. 2016), which uses colour selection to identify passive galaxies that allow precise photometric redshifts. To model a colour-selected sample, we also extend the usual HOD formulation to include a parameter that allows for 'central galaxy incompleteness,' i.e. for high-mass haloes that do not contain central galaxies passing the sample's colour cuts.

We adopt this HOD framework to populate *N*-body simulations from the AbacusCosmos suite (Garrison et al. 2018) in order to model the GGL excess surface density $\Delta\Sigma(r_p)$ and projected galaxy correlation function $w_{p,\,gg}(r_p)$ on scales $0.3\,h^{-1}$ Mpc $< r_p <$ $30.0\,h^{-1}$ Mpc as a function of HOD and wCDM cosmological parameters. To accurately model this datavector down to small scales, we adopt and extend the Gaussian process emulation scheme of Wibking et al. (2020). This emulation is done over a large HOD and cosmological parameter space centred on a fiducial model that roughly describes the high-density DES redMaGiC sample. We use this emulator to compute derivatives of $\Delta\Sigma$ and $w_{p,\,gg}$ with respect to HOD and cosmological parameters, which we then use to forecast a cosmological analysis of DES redMaGiC GGL and clustering. We devote particular attention to the importance of the small scales in such an analysis and also to the ability of the datavector to break the degeneracy between cosmology and systematic uncertainties in lensing calibration. The technical development behind producing our forecasts is aimed at enabling a fully non-linear GGL and clustering analysis of the final DES data release, which we predict to yield per cent-level constraints on the amplitude of matter clustering.

Our forecasts could prove optimistic if observational or theoretical systematics in the final DES data turn out to be larger than we have assumed. For example, the Y3 cosmology analysis identifies systematics in the clustering measurements of the redMaGiC sample (DES Collaboration 2021), while we have assumed that systematic uncertainties in $w_{p,\,gg}$ will be negligible. None the less, our forecasts play a valuable role in demonstrating what DES GGL+clustering should be able to achieve if systematics are well controlled, thus also demonstrating the level of systematics control that is required. A key finding of our analysis is that modelling GGL + clustering into non-linear scales can achieve gains in cosmological parameter precision that are equivalent factors of 2.5−8.0 increases in survey area, e.g. to the difference between a 5-yr weak lensing survey and a survey lasting one to several decades. Doing the additional work needed to realize these gains is a promising investment.

The next section describes our numerical simulations and HOD modelling methodology. Section 3 defines our clustering and lensing statistics, then describes our emulation methodology and derives the sensitivity of our datavector to HOD and cosmological parameters. Section 4 describes how we compute covariance matrices for our Fisher forecasts, based on expectations for the final DES data release. In Section 5 we present our main forecast results, which combine the derivatives computed in Section 3.3 with the covariance matrices of Section 4 to derive constraints on Ω_m, σ_8, and S_8. We summarize our results and conclude in Section 6.

2 CONSTRUCTING MOCK GALAXY CATALOGUES

2.1 Simulations and halo identification

We use 40 AbacusCosmos simulations in our analysis (Garrison et al. 2018). These simulations are run with a variety of wCDM cosmologies centred on the Planck Collaboration XIII (2016) cosmology with fixed phases. The 40 cosmologies are selected using a Latin hypercube method (Heitmann et al. 2009) optimized to maximize the distance between points. These cosmologies are sampled from a parameter space consisting of the union of cosmic microwave background (CMB), baryon acoustic osccilations (BAO), and supernovae (SN) results described in Anderson et al. (2014). We utilize the larger 1100.0 h^{-3} Mpc^3 set of boxes with mass resolution of 10^{10} $M_\odot\,h^{-1}$.

Haloes were identified from particle snapshots using the software package ROCKSTAR version 0.99.9-RC3 + (Behroozi, Wechsler & Wu 2013). We use strict (i.e. without unbinding) spherical overdensity (SO) halo masses around the halo centres identified by ROCKSTAR, rather than the default phase-space FOF-like masses output by ROCKSTAR. For finding haloes ROCKSTAR uses a primary

[1] We use ΛCDM to denote a model with inflationary primordial fluctuations, cold dark matter, a cosmological constant, and a flat universe.

definition set to the virial mass of Bryan & Norman (1998). However, after identification, we adopt the M_{200b} mass definition, i.e. the mass enclosed by a spherical overdensity of 200 times the mean matter density at a given redshift and cosmology. Distinct haloes identified with the $M_{\rm vir}$ definition are not reclassified as subhaloes under the M_{200b} definition; such reclassification would affect a negligible fraction of haloes. We identify haloes above 20 particles, and we only use distinct haloes (not subhaloes) when creating galaxy populations.

2.2 HOD modelling

Similar to our previous papers we populate simulated haloes with galaxies according to a halo occupation distribution (HOD) framework (e.g. Jing et al. 1998; Benson et al. 2000; Ma & Fry 2000; Peacock & Smith 2000; Seljak 2000; Scoccimarro et al. 2001; Berlind & Weinberg 2002; Cooray & Sheth 2002; van den Bosch, Yang & Mo 2003; Yang, Mo & van den Bosch 2003; Zheng et al. 2005; Cooray 2006; Mandelbaum et al. 2006; Zheng et al. 2009; Zehavi et al. 2011; Coupon et al. 2012; Leauthaud et al. 2012; Guo et al. 2014; Zu & Mandelbaum 2015; Zehavi et al. 2018). We extend this framework to include central incompleteness, galaxy assembly bias, and the possibility for the galaxy profile to deviate from that of its host's matter profile. We parametrize the mean central and satellite occupations of our haloes with a modified form of the widely used equations (Zheng et al. 2005),

$$\langle N_{\rm cen}(M_h)\rangle = \frac{f_{\rm cen}}{2}\left[1+{\rm erf}\left(\frac{\log M_h - \log M_{\rm min}}{\sigma_{\log M}}\right)\right], \quad (1)$$

$$\langle N_{\rm sat}(M_h)\rangle = \frac{\langle N_{\rm cen}(M_h)\rangle}{f_{\rm cen}}\left(\frac{M_h - M_0}{M_1}\right)^{\alpha}. \quad (2)$$

The new parameter $f_{\rm cen}$ allows only a fraction of high-mass haloes to contain central galaxies that satisfy the sample selection criteria. Incompleteness may be present in any galaxy sample, but is particularly important for us to model because we are forecasting for an analysis that utilizes redMaGiC (Rozo et al. 2016) selected galaxies. These galaxies are known to exhibit central incompleteness because of the strict colour cuts applied in their selection. The fraction of satellite galaxies that pass selection criteria is already encoded within the parameter M_1.

The actual numbers of centrals and satellites placed into each halo is drawn randomly from binomial and Poisson distributions, respectively, with the mean occupations given above. Centrals are placed at the center of their host halo, while satellites are distributed according to a Navarro–Frenk–White profile (NFW; Navarro, Frenk & White 1997),

$$\rho_{\rm gal}(r) = \rho_m(r|A_{\rm con}\times c_{\rm vir}), \quad (3)$$

parametrized by halo concentration $c_{\rm vir} = r_h/r_s$ with the parameter $A_{\rm con}$ included to allow for the galaxy profile to deviate from that of the matter. As in Salcedo et al. (2020b), we use the fits of Correa et al. (2015) to assign halo concentrations because they were calibrated using significantly higher resolution simulations than our AbacusCosmos boxes.

Following Wibking et al. (2019; see also McEwen & Weinberg 2018; Salcedo et al. 2020b; Xu et al. 2021) we allow for the possibility of galaxy assembly bias. Galaxy assembly bias refers to the possibility for galaxy occupation at fixed host halo mass to depend on properties other than halo mass. In combination with *halo* assembly bias, this can boost the large-scale clustering of galaxies (e.g. Croton et al. 2007; Zu et al. 2008), and it represents an important source of systematic uncertainty in current cosmological analyses. It is currently unclear which halo internal property, if any, is responsible for galaxy assembly bias. However, in the context of a cosmological analysis, in which assembly bias is treated as a nuisance effect to be marginalized over, it is only important to *characterize* its potential effects. Therefore, we choose to allow the central and satellite occupations to vary on a halo-by-halo basis based on the matter overdensity measured in a top-hat spheres of radius $8.0\,h^{-1}$ Mpc centred on each individual halo δ_8^m. This environmental dependence is written as

$$\log M_{\rm min} = \log M_{\rm min,0} + Q_{\rm cen}(\tilde{\delta}_8^m - 0.5), \quad (4)$$

$$\log M_1 = \log M_{1,0} + Q_{\rm sat}(\tilde{\delta}_8^m - 0.5), \quad (5)$$

where $Q_{\rm cen}$ and $Q_{\rm sat}$ express the strength of the dependence of $M_{\rm min}$ and M_1, respectively, on environment and $\tilde{\delta}_8^m \in [0,1]$ is the normalized rank of δ_8^m within a narrow mass bin. In this parametrization the case of $Q_{\rm cen} = Q_{\rm sat} = 0.0$ corresponds to having no assembly bias. This parametrization has been found to provide a reasonable description of galaxy assembly bias effects in semi-analytic models and hydrodynamic simulations (e.g. Artale et al. 2018; Zehavi et al. 2018; Bose et al. 2019; Contreras et al. 2019; Xu et al. 2021). Despite this success we note that further work is required to establish the optimal scale at which the overdensity is measured to implement galaxy assembly bias in an HOD context or if a model that more flexibly combines information from multiple scales is necessary.

The Y3 DES 3 × 2pt. cosmological analysis (DES Collaboration 2021) considered both the redMaGiC galaxy sample and an apparent magnitude-limited sample (Porredon et al. 2021), adopting the latter for its fiducial results. We expect that our HOD parametrization would adequately represent this magnitude-limited sample, but the fiducial parameters would be quite different from those for redMaGiC, with higher $n_{\rm gal}$, higher $f_{\rm cen}$, shallower α, and perhaps smaller $\sigma_{\log M}$, based on SDSS results at low redshift (Zehavi et al. 2011). Because of the higher $n_{\rm gal}$, the magnitude-limited sample should yield smaller statistical errors, particularly for $\Delta\Sigma$, and might therefore achieve tighter statistical constraints than those forecast here. However, there are additional complications in modelling this sample because of the lower precision of photometric redshifts, and we have not investigated the impact of these complications.

3 EMULATION OF COSMOLOGICAL OBSERVABLES

3.1 Clustering and weak-lensing statistics

We use CORRFUNC (Sinha & Garrison 2017) to compute the real-space galaxy autocorrelation function $\xi_{gg}(r_p,\pi)$ and galaxy-matter cross-correlation function $\xi_{gm}(r_p,\pi)$ in 20 equal logarithmically spaced bins of r_p covering scales $0.3 < r_p < 30.0\ h^{-1}$ Mpc and 100 equal linearly spaced bins out to $\Pi_{\rm max} = 100.0\ h^{-1}$ Mpc. These real-space correlation functions are used to calculate the more observationally motivated quantities $w_{p,gg}(r_p)$ and $\Delta\Sigma(r_p)$,

$$w_{p,AB}(r_p) = 2\int_0^{\Pi_{\rm max}} \xi_{AB}(r_p,\pi), \quad (6)$$

$$\Delta\Sigma(r_p) = \Omega_m\rho_{\rm crit}\left[\frac{2}{r_p^2}\int_0^{r_p} r' w_{p,gm}(r')dr' - w_{p,gm}(r_p)\right]. \quad (7)$$

For a given source redshift distribution, $\Delta\Sigma(r_p)$ is proportional to the observable tangential shear profile,

$$\gamma_t(r_p) = \frac{\Delta\Sigma(r_p)}{\Sigma_{\rm crit}}, \quad (8)$$

where the critical surface density $\Sigma_{\rm crit}$ is

$$\Sigma_{\rm crit} = \frac{c^2}{4\pi G}\frac{H(z_{\rm src}-z_{\rm lens})D_c(z_{\rm src})}{D_c(z_{\rm lens})\left[D_c(z_{\rm src})-D_c(z_{\rm lens})\right](1+z_{\rm lens})}, \quad (9)$$

and where $D_c(z)$ denotes the comoving distance to redshift z with the Heaviside step function H enforcing the convention that $\Sigma_{\rm crit}(z_{\rm src} < z_{\rm lens}) = 0$.

Errors in photometric redshift estimation can introduce errors into $\Sigma_{\rm crit}$ and therefore $\Delta\Sigma$. Additionally, errors in shear calibration will introduce errors in $\Delta\Sigma$ through γ_t. We characterize the effect of these errors by introducing a scale-independent lensing bias parameter $A_{\rm lens}$,

$$\Delta\Sigma_{\rm obs}(r_p) = A_{\rm lens} \times \Delta\Sigma_{\rm true}(r_p). \quad (10)$$

We include $A_{\rm lens}$ as an additional nuisance parameter that we marginalize over in our forecasts in Section 5. The DES Y3 analysis finds evidence of internal inconsistency between the clustering and GGL of redMaGiC galaxies, which they tentatively ascribe to an undiagnosed systematic in the clustering measurements (DES Collaboration 2021; Pandey et al. 2021). They model this effect with a nuisance parameter $X_{\rm lens}$ that scales the predicted GGL signal relative to clustering, inferring a value $X_{\rm lens} \approx 0.9$ rather than the theoretically expected 1.0. We suspect that our forecasts would be similar if we replaced $A_{\rm lens}$ with $X_{\rm lens}$ as a nuisance parameter *and* adopted the same fractional prior (3 per cent in our fiducial case). However, we have not investigated this alternative parametrization of systematics. Our forecasts implicitly assume that the systematics suggested by Y3 redMaGiC galaxy clustering will be controlled in the final analysis, at least to the level represented by our $A_{\rm lens}$ prior.

In addition to a multiplicative lensing bias, so-called 'boost' factors will also affect the galaxy–galaxy lensing signal of redMaGiC galaxies. These are a correction to the measured lensing signal to account for the presence of lens-source clustering. In the case of redMaGiC galaxies, boost factors significantly impact the small-scale lensing signal, but their uncertainties are relatively small (e.g. Prat et al. 2021) and subdominant to our statistical errors. Therefore, we do not model boost factors for our forecast analysis.

Our choice to model the projected correlation function of redMaGiC selected galaxies is somewhat idiosyncratic, since these galaxies have photometrically estimated redshifts. Photometric samples are more commonly characterized by the angular correlation function in photo-z bins, whereas $w_{p,\,gg}$ uses the photo-z's of each pair of galaxies to estimate the separations of r_p and π. The redMaGiC algorithm produces impressively precise photometric redshifts in the redshift range $z = 0.1-0.7$, roughly 1–2 per cent in terms of $1 + z_{\rm phot}$ (Rozo et al. 2016). Given our fiducial cosmology, this precision corresponds to 30.0–60.0 h^{-1} Mpc errors in line-of-sight distance. Because we integrate to $\Pi_{\rm max} = 100.0\,h^{-1}$ Mpc, the photo-z errors will mildly depress $w_{p,\,gg}(r_p)$ by a scale-independent factor (Wang et al. 2019). In this paper we ignore this effect, implicitly taking for granted our ability to model it with good enough knowledge of photo-z errors, and assuming its independence from HOD and cosmology. We examine this problem more fully in a forthcoming paper (Zeng et al. in prep.).

To model the dependence of $w_{p,\,gg}$ on our HOD and cosmological parameters we choose to directly emulate a halo-model correction (Wibking et al. 2020),

$$f_{\rm corr}(r_p) = \frac{w^{\rm sim}_{p,gg}(r_p)}{w^{\rm model}_{p,gg}(r_p)}, \quad (11)$$

where $w^{\rm sim}_{p,gg}$ is calculated using CORRFUNC on our simulation mock galaxy catalogues, and $w^{\rm model}_{p,gg}$ is analytically calculated. This procedure has two major advantages, the first being that the ratio $f_{\rm corr}$ has a significantly smaller dynamic range than $w^{\rm sim}_{p,gg}$. Additionally, $w^{\rm model}_{p,gg}$ is capable of capturing a significant amount of the sensitivity to our HOD and cosmological parameters with insignificant computational expense. The upshot is that our emulation scheme is able to more accurately fit $f_{\rm corr}$ than $w^{\rm sim}_{p,gg}$. For galaxy–galaxy lensing, on the other hand, we have found that we can achieve acceptable modelling errors when emulating $\Delta\Sigma$ directly. This success may not hold for a different set of modelling requirements (e.g. a larger survey that yields smaller measurement errors), in which case we could emulate a similar halo-model correction for $\Delta\Sigma$.

To calculate $w^{\rm model}_{p,gg}$ we integrate over an analytically calculated real-space galaxy autocorrelation function $\xi^{\rm model}_{gg}$, which is expressed as a quadrature sum of 1- and 2-halo terms,

$$\xi^{\rm model}_{gg}(r) = \sqrt{\left(\xi^{\rm 1h}_{gg}\right)^2 + \left(\xi^{\rm 2h}_{gg}\right)^2}. \quad (12)$$

The two-halo term is given by,

$$\xi^{\rm 2h}_{gg} = b_g^2 \times \xi_{mm}(r), \quad (13)$$

where ξ_{mm} is the linear theory matter–matter correlation function and b_g is the galaxy-bias calculated by integrating over the HOD and halo-mass function $\mathrm{d}n_h/\mathrm{d}M_h$ and halo bias function $b_h(M_h)$,

$$b_g = \frac{1}{n_{\rm gal}}\int_0^\infty \mathrm{d}M_h \frac{\mathrm{d}n_h}{\mathrm{d}M_h} < N(M_h) > b_h(M_h). \quad (14)$$

The more complicated 1-halo term is a sum of central–satellite DD_{cs} and satellite–satellite DD_{ss} pairs,

$$1 + \xi_{gg}(r) = \frac{DD_{cs}(r) + DD_{ss}(r)}{RR(r)}, \quad (15)$$

where $RR(r) = 2\pi r^2 n_g$. These terms are written as,

$$DD_{cs}(r) = \int_0^\infty \langle N_{\rm cen}(M_h)\rangle\langle N_{\rm sat}(M_h)\rangle I'\left(\frac{r}{r_h(M_h)}, c_{\rm vir}(M_h)\right) \times \frac{\mathrm{d}n_h}{\mathrm{d}M_h}\frac{1}{r_h(M_h)}\mathrm{d}M_h, \quad (16)$$

$$DD_{ss}(r) = \frac{1}{2}\int_0^\infty \langle N_{\rm sat}(M_h)\rangle^2 F'\left(\frac{r}{r_h(M_h)}, c_{\rm vir}(M_h)\right) \times \frac{\mathrm{d}n_h}{\mathrm{d}M_h}\frac{1}{r_h(M_h)}\mathrm{d}M_h, \quad (17)$$

where I' and F' are dimensionless, differential pair count functions for an NFW profile. In the interest of brevity we omit expressions for these terms and direct the reader to the appendices of Wibking et al. (2020) for them. In the calculation of the 1- and 2-halo terms we utilize the mass function $\mathrm{d}n_h/\mathrm{d}M_h$ of Tinker et al. (2008), the halo bias function $b_h(M_h)$ of Tinker et al. (2010), and the redshift-dependent concentration–mass relation of Correa et al. (2015). The matter–matter correlation function ξ_{mm} is obtained by Fourier transforming the linear matter power spectrum calculated with the fitting formula of Eisenstein & Hu (1998). Although this calculation of $\xi^{\rm model}_{gg}$ would not be accurate enough on its own for DES analysis, it allows us to construct a high-accuracy emulator.

3.2 Emulation using Gaussian processes

To model the dependence of $w_{p,\,gg}$ and $\Delta\Sigma$ on cosmological and HOD parameters, we implement the Gaussian process emulation scheme of Wibking et al. (2020). This amounts to performing a Gaussian process regression with a squared-exponential kernel in each radial bin of $f_{\rm corr}$=$w^{\rm sim}_{p,gg}/w^{\rm model}_{p,gg}$ and $\Delta\Sigma$. In each bin the

Table 1. Fiducial model parameters (HOD and cosmological).

Parameter	Fiducial value	Sampling range	Description
$n_{\rm gal} \times 10^3$	1.0 h^3 Mpc^{-3}	[0.8, 1.2] × h^3 Mpc^{-3}	galaxy number density
$\sigma_{\log M}$	0.6	[0.4, 0.8]	width of central occupation cutoff
$\frac{M_1}{M_{\rm min}}$	30.0	[20.0, 50.0]	satellite fraction parameter
$\frac{M_0}{M_1}$	0.2	–	satellite cutoff parameter
α	1.5	[1.2,1.8]	slope of satellite occupation power law
$f_{\rm cen}$	0.6	[0.4, 0.8]	central incompleteness factor
$A_{\rm con}$	1.0	[0.5, 2.0]	galaxy concentration factor
$Q_{\rm cen}$	0.0	[−0.3, 0.3]	central galaxy assembly bias parameter
$Q_{\rm sat}$	0.0	[−0.3, 0.3]	satellite galaxy assembly bias parameter
$A_{\rm lens}$	1.0	–	scale independent lensing bias parameter
Ω_m	0.314	[0.253, 0.367]	cosmological matter density
σ_8	0.83	[0.65, 1.0]	power spectrum amplitude
H_0	67.26	[61.567, 74.793]	Hubble constant
w_0	−1.00	[−1.370, −0.655]	equation of state of dark energy
n_s	0.9652	[0.9300, 0.9898]	scalar spectral index

hyperparameters of the kernel are obtained by maximizing the leave-one-out cross validation pseudo-likelihood. For more details on this process we direct the reader to the relevant appendices in Wibking et al. (2020).

The input data for this emulation are computed from 1000 cosmology and HOD models obtained from assigning 25 randomly generated HOD models to each of the 40 AbacusCosmos simulations described in Section 2.1. The cosmological models used in these 40 simulations are drawn from constraints from CMB, BAO, and SN data (Anderson et al. 2014) using the Latin hypercube sampling method of Heitmann et al. (2009). To obtain HOD parametrizations we Latin hypercube sample over flat probability density distributions in the ranges given in Table 1.[2] While not strictly necessary in a forecast context, these ranges are chosen to produce a large volume in parameter space to demonstrate the utility of our emulation scheme. Also listed in Table 1 are fiducial values of each parameter chosen to roughly describe the high-density sample of redMaGiC galaxies. We use these fiducial values to compute derivatives with respect to our combined HOD and cosmological parameter vector. We produce 1000 HOD parametrizations using this method and randomly assign 25 to each of the 40 AbacusCosmos cosmologies without replacement. For each combination of HOD and cosmology we compute $f_{\rm corr}$ and $\Delta\Sigma$ as described in Section 3.1. The set of 1000 $f_{\rm corr}$ and $\Delta\Sigma$ models serves as the input to our Gaussian process emulator.

In Fig. 1 we show the input data set for emulation (top panels) of $f_{\rm corr}$ and $\Delta\Sigma$ as well as the respective modelling errors we obtain (bottom panels). The left-hand panels correspond to $\Delta\Sigma$ while the right-hand panels correspond to $w_{p,\,gg}$. Each top panel shows the fiducial model in black with 1000 additional faint lines representing the models we use to construct our emulator. We can see that the parameter space we model covers a large range in amplitude for both of our observables. Each bottom panel shows the respective leave-one-out-simulation error. This error is computed by training the emulator with all elements of the training set except for those associated with one of the 40 AbacusCosmos boxes, then comparing it to the observable computed with that simulation (cosmology) and HOD parametrization. This functions as a conservative estimate of the accuracy of our emulator. The yellow region in each panel shows the diagonal errors we assume for our forecast of DES-Y6 clustering and galaxy–galaxy lensing. We can see that for both $w_{p,\,gg}$ and $\Delta\Sigma$ our modelling errors are comparable to the statistical errors. For $w_{p,\,gg}$ we can see that the 1σ errors are noticeably larger than the 15th/85th error percentiles at small scales indicating that the errors are non-Gaussian. The outliers in error space are also outliers in $w_{p,\,gg}$ space, so the 15th/18th percentile curves are more indicative of modelling errors that would appear in a likelihood analysis of data. Furthermore, the range of models being emulated is much larger than the $\pm 5\sigma$ range expected from the DES errors, and training and applying the emulator over a more restricted range compatible with the measurements would yield still smaller emulator errors. We conclude that the current emulator is probably accurate enough to model $\Delta\Sigma$ and $w_{p,\,gg}$ in the final DES data, at least within our adopted parametric model, though further testing in the context of the final measurements will be desirable.

3.3 Cosmological and HOD derivatives

To compute derivatives for use in our Fisher forecast analysis, we use our emulator to compute $w_{p,\,gg}$ and $\Delta\Sigma$ at the fiducial values listed in Table 1 and steps up and down in each of our parameters. When using these derivatives to compute forecast constraints we additionally smooth them with a Savitsky–Golay filter. Rather than plot the derivatives directly, in Fig. 2 we instead examine the impact of fixed variations in parameters for $w_{p,\,gg}$ and $\Delta\Sigma$. Curves in the figure are computed using simulations (snapshots at $z = 0.5$). In each panel red (blue) curves show the effect of increasing (decreasing) the indicated parameter relative to the fiducial value for $\Delta\Sigma$ (solid lines) and $w_{p,\,gg}$ (dashed lines).

We begin by examining the effects of parameter changes on $\Delta\Sigma$. We see that a decrease in the galaxy number density $n_{\rm gal}$ corresponds to an increase in $\Delta\Sigma$ at all scales. Recall that we treat $n_{\rm gal}$ as an adjustable HOD parameter, not $M_{\rm min}$, so when we reduce $n_{\rm gal}$ we increase $M_{\rm min}$ and M_1 at fixed $M_1/M_{\rm min}$ to achieve the new density. At small scales this has a significant effect on $\Delta\Sigma$ by increasing the mean mass of haloes that host galaxies. At large scales this increase in mean host halo mass leads to a small-scale independent increase

[2]Note that in our HOD analysis we choose to consider the galaxy number density $n_{\rm gal}$ as a parameter because it provides a direct observational constraint on the HOD. Consequently, we do not consider $M_{\rm min}$, M_1, or M_0 directly as parameters but instead model the ratios $M_1/M_{\rm min}$ and M_0/M_1.

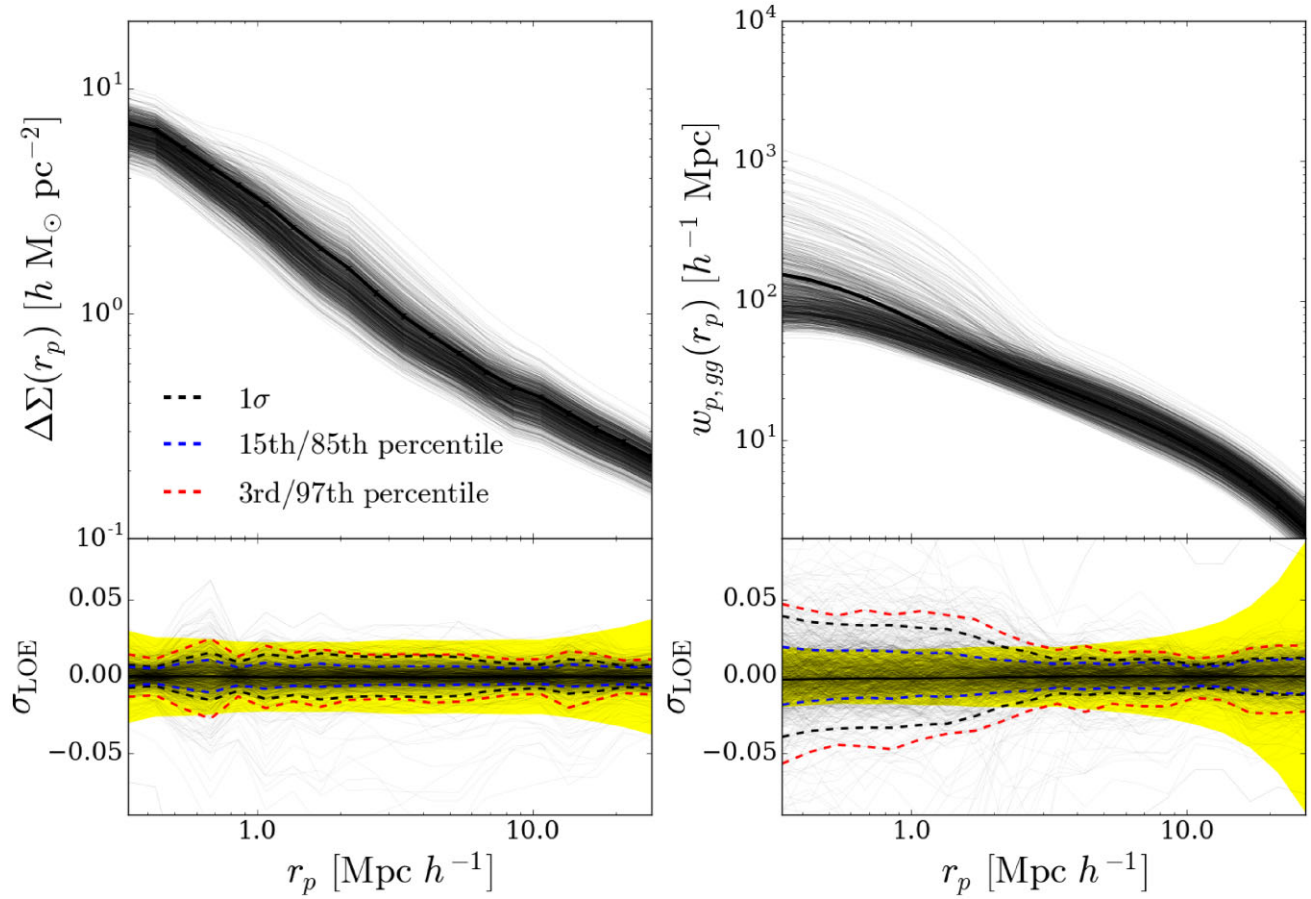

Figure 1. $\Delta\Sigma$ (left) and $w_{p,\,gg}$ (right) as predicted by our simulations in our $z = 0.5$ bin. Each of the grey-scale lines plots one of the 1000 training HOD + cosmology models we use to compute our emulator, while the black line shows the prediction for our fiducial model. The respective bottom panels show the leave-one-out emulator error for our two observables compared with the predicted observable covariance, plotted as a yellow band.

in the galaxy bias. Turning to $\sigma_{\log M}$ we see that an increase in the parameter decreases $\Delta\Sigma$ at all scales. At large scales this behaviour is similar to the case of raising $n_{\rm gal}$: an increase in $\sigma_{\log M}$ corresponds to a decrease in the mean host halo mass and therefore the galaxy bias. At small scales the increase in $\sigma_{\log M}$ leads to a decrease in the satellite fraction. This small-scale sensitivity exhibits an interesting scale dependence, peaking around $1.0-2.0\,h^{-1}$ Mpc, due to the offset in the positions of satellites and the peak of the matter distribution at the center of the host halo.

The parameters $M_1/M_{\rm min}$ and α exhibit very similar behaviour. Increasing (decreasing) α ($M_1/M_{\rm min}$) increases the galaxy bias and satellite fraction, leading to a boost to the amplitude of $\Delta\Sigma$ at all scales. We note that the extent to which the satellite fraction is increased due to changes in M_1 and $M_{\rm min}$ at fixed $M_1/M_{\rm min}$ depends on the value of α. Because α is relatively high, with a fiducial value of 1.5, a decrease in M_1 contributes relatively more satellites than an equal decrease in $M_{\rm min}$ contributes centrals. Depending on the shape of the halo mass function, a lower value of α could reverse this situation.

The remaining HOD parameters $f_{\rm cen}$, $A_{\rm con}$, $Q_{\rm cen}$, and $Q_{\rm sat}$ exhibit more interesting behaviour. When $f_{\rm cen}$ is decreased this boosts the large scales of $\Delta\Sigma$ by increasing the satellite fraction (since $n_{\rm gal}$ is held fixed) and therefore the galaxy bias. However, at the smallest scales this leads to a decrease in $\Delta\Sigma$. This is because central galaxies residing in the most massive haloes contribute significantly to $\Delta\Sigma$. Unlike changes in the satellite fraction due to $\sigma_{\log M}$ or $M_1/M_{\rm min}$, changing $f_{\rm cen}$ removes some of these high-signal central galaxies. An increase in the parameter $A_{\rm con}$ increases the concentration of satellite galaxies. This moves satellites closer to the peak of the matter distribution within haloes and therefore increases the 1-halo term of $\Delta\Sigma$. Because $A_{\rm con}$ does not affect the mean occupation at all, it has no effect on large scales.

Turning to the first of our assembly bias parameters we see that a decrease in $Q_{\rm cen}$ boosts $\Delta\Sigma$ at all scales. This is because negative values of $Q_{\rm cen}$ decrease $M_{\rm min}$ for haloes in dense environments. This leads to a significant increase in $\Delta\Sigma$ at large scales peaking around $8.0\,h^{-1}$ Mpc. The effect decreases towards small scales, though it does not vanish. Similarly a decrease in $Q_{\rm sat}$ decreases M_1 for haloes in dense environments, boosting $\Delta\Sigma$ at all scales. Interestingly, $Q_{\rm sat}$ has a much smaller effect on $\Delta\Sigma$ than $Q_{\rm cen}$. This is because the variation in bias for low-mass haloes that may host a central is much larger than for the high-mass haloes that host satellites.

Next are our cosmological parameters. We see that an increase in Ω_m leads to an increase in $\Delta\Sigma$ at all scales, with some mild scale dependence at small scales. The effect of increasing Ω_m on the linear power spectrum is to shift it towards higher k, or equivalently to shift ξ_{mm} towards lower r. This leads to a decrease in ξ_{mm} at large scales and an increase at small scales that is suppressed by non-linear evolution. The large scale decrease is counteracted and overcome by the increase in the $\Omega_m\rho_{\rm crit}$ pre-factor in $\Delta\Sigma$, and the increase in $\Delta\Sigma$ at small scales is larger still. Increasing σ_8 also increases $\Delta\Sigma$ at all scales though with a different scale dependence that peaks at

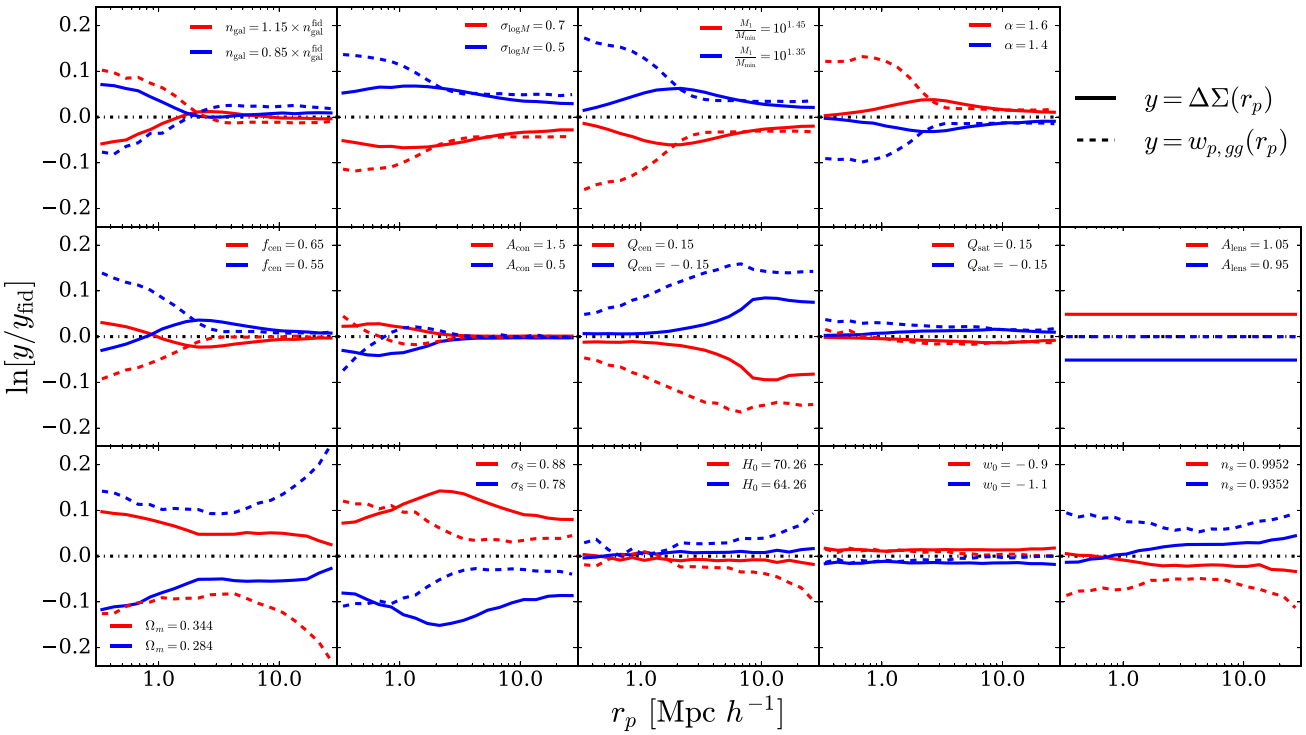

Figure 2. Fractional changes to $\Delta\Sigma$ (solid lines) and $w_{p,gg}$ (dashed lines) induced by changes in HOD and cosmological parameters at $z = 0.5$. In each panel red and blue curves show the emulator-predicted change of the observable for the parameter values indicted in the panel legend while holding all other parameters fixed.

$r_p \approx 2.0$–$3.0\,h^{-1}$ Mpc. This is directly due to an increase in ξ_{mm} at all scales. An increase in H_0, like an increase in Ω_m, shifts the linear power spectrum towards higher k, and the impact on the $\Omega_m\rho_{\rm crit}$ pre-factor is absorbed by measuring $\Delta\Sigma$ in units of h^{-1} $M_\odot$ pc^2. The impact is a small decrease in $\Delta\Sigma$ at large r_p. Note that when we compute derivatives with respect to σ_8 we use the value of σ_8 at $z = 0$ rather than the relevant snapshot redshift. In principle, this choice can affect our constraints, but in practice the effect is small.

Increasing w_0 from -1.0 to -0.9 leads to a slight scale independent increase in $\Delta\Sigma$, which is due to the analogous increase in ξ_{mm}. With $w_0 = -0.9$, structure growth 'freezes' at slightly higher redshift, and with σ_8 fixed at $z = 0$ the implied clustering at $z > 0$ is larger. Increasing n_s makes the linear power spectrum bluer, decreasing the large scale ξ_{mm} (and thus $\Delta\Sigma$) relative to the $8.0\,h^{-1}$ Mpc scale. The converse effect on small scales is damped by non-linear evolution.

Turning to $w_{p,gg}$, we see similar behaviour as $\Delta\Sigma$ for many of our HOD parameters, particularly at large scales. As discussed in the $\Delta\Sigma$ case, the most important effect an HOD parameter can have on large scales is to change the galaxy bias by changing the mean host halo mass. We can see this in the case of $n_{\rm gal}$, $\sigma_{\log M}$, $M_1/M_{\rm min}$, α, and $f_{\rm cen}$, where the effects on the large scales of $w_{p,gg}$ of our parameter variations are qualitatively similar to those for $\Delta\Sigma$. There are subtle differences in scale dependence at large scales due to the fact that $\Delta\Sigma$ is an *excess* surface density rather than a local overdensity. At small scales there are more significant differences between $w_{p,gg}$ and $\Delta\Sigma$ because of the strong impact of the satellite fraction on ξ_{gg} in the 1-halo regime. For $n_{\rm gal}$ the small-scale effect is opposite in sign to the large-scale effect because the increase of satellite galaxies dominates over the reduction in the galaxy bias. Our next three parameters, $\sigma_{\log M}$, $M_1/M_{\rm min}$, and α, exhibit similar small-scale behaviour because they all also increase the satellite fraction at fixed $n_{\rm gal}$.

In contrast the central incompleteness parameter $f_{\rm cen}$ exhibits significantly different behaviour at small scales than $\Delta\Sigma$. Because $w_{p,gg}$ includes a satellite–satellite contribution to the 1-halo term, increasing the satellite fraction with a reduced $f_{\rm cen}$ at fixed $n_{\rm gal}$ leads to an increase in the 1-halo term at all scales. Turning to $A_{\rm con}$ we see further differences in small-scale behaviour. An increase in $A_{\rm con}$ boosts the very smallest scales of $w_{p,gg}$ but has a compensatory decrease at larger scales still within the 1-halo term. This is because the pairs gained at small scales by sharpening the galaxy profile concentration are lost at larger scales.

Our assembly bias parameters also exhibit different behaviour than in the case of $\Delta\Sigma$. A decrease of $Q_{\rm cen}$ increases $w_{p,gg}$ at all scales but does so more significantly than for $\Delta\Sigma$. We also observe the same peak around $8.0\,h^{-1}$ Mpc, but it is much smoother. The satellite assembly bias parameter $Q_{\rm sat}$ exhibits similar behaviour for $w_{p,gg}$ and $\Delta\Sigma$ at large scales, but it differs at small scales. Interestingly, both a decrease and increase of $Q_{\rm sat}$ boost the small scales of $w_{p,gg}$. This is because we have chosen for our fiducial value $Q_{\rm sat} = 0.0$, which minimizes the value of the second moment of the halo occupation $\langle N^2_{\rm gal}(M_h)\rangle$.

The effect of our cosmological parameters on $w_{p,gg}$ is in most cases similar to the effect on $\Delta\Sigma$, albeit with different detailed scale dependence. The notable exceptions are Ω_m and n_s at small scales. Unlike the case of $\Delta\Sigma$, an increase in Ω_m leads to a decrease in $w_{p,gg}$ because there is no longer a pre-factor proportional to Ω_m. The small-scale behaviour follows from the upward shift in the halo mass function caused by higher Ω_m. To achieve the same number density at fixed $M_1/M_{\rm min}$, both M_1 and $M_{\rm min}$ must shift to

high values. As discussed previously this leads to a decrease in the satellite fraction and therefore depresses the 1-halo term. The origin of the small-scale impact of n_s is not obvious, but we suspect it derives from the effect of the power spectrum shape on the halo mass function.

3.4 Summary

Regardless of the detailed explanations of each curve in Fig. 2, our critical finding is that each parameter that has a significant impact on $\Delta\Sigma$ or $w_{p,\,gg}$ does so with a distinct scale dependence, which is typically different for the two observables. Therefore, even though the HOD introduces many free parameters, precise measurements of $\Delta\Sigma$ and $w_{p,\,gg}$ over a wide dynamic range provide enough information to break parameter degeneracies and achieve tight constraints on cosmological parameters. The distinctive scale dependence arises because we span the linear, trans-linear, and fully non-linear regimes. Modelling measurements into small scales thus offers the prospect of significantly improving cosmological inferences from weak lensing and galaxy clustering data, as we demonstrate in subsequent sections.

4 COVARIANCE ESTIMATION

We use a combination of analytic and numerical methods to compute the observable covariance matrix for $w_{p,\,gg}$ and $\Delta\Sigma$. We analytically compute the $\Delta\Sigma$ covariance using a Gaussian formalism, i.e. assuming the galaxy and matter fields are Gaussian random and adding a shape noise contribution (e.g. Singh et al. 2017; Wibking et al. 2020). Recently, Wu et al. (2019), in the context of cluster weak lensing, showed that the standard Gaussian formalism for computing the lensing covariance becomes insufficient when the large-scale structure contribution to the covariance becomes comparable to shape noise. Because our $\Delta\Sigma$ covariance is shape-noise dominated we utilize the standard Gaussian formalism, but we note that in a deeper weak lensing survey than DES it may become insufficient for galaxy–galaxy lensing as well. Because the lensing covariance matrix is shape-noise dominated, we also ignore the cross-observable covariance with $w_{p,\,gg}$ and treat the two observables as independent in all that follows.

We include a correction to the $\Delta\Sigma$ covariance matrix to analytically marginalize over potential contributions from a point mass at the center of each galaxy lens (e.g. MacCrann et al. 2020; Wibking et al. 2020). This enclosed point mass, which is allowed to be positive or negative, can represent the impact of small-scale substructure that is unresolved and absent from our simulations. It can also characterize the impact of baryonic physics effects like dissipation and feedback. In the covariance matrix, the point-mass correction takes the form,

$$\tilde{C} = C + \sigma^2 v v^T, \tag{18}$$

where v is a column vector with values $\left[r_{p,0}^{-2}, r_{p,1}^{-2}, ..., r_{p,N}^{-2}\right]$ and σ is the width of the Gaussian prior on the enclosed point mass. We use the Sherman–Morrison matrix identity and assume a flat prior on σ (e.g. MacCrann et al. 2020; Wibking et al. 2020), yielding

$$\tilde{C}^{-1} = C^{-1} - \frac{C^{-1} v v^T C^{-1}}{v^T C^{-1} v}. \tag{19}$$

To compute the covariance for $w_{p,\,gg}$, we use a combination of analytic and numerical methods. Unlike $\Delta\Sigma$ the covariance for $w_{p,\,gg}$ contains a significant non-Gaussian contribution, particularly at small scales.[3] To account for this contribution we use bootstrap methods to numerically compute the covariance using the 20 $(1100.0\ h^{-1}\ \mathrm{Mpc})^3$ simulation boxes of a fiducial cosmology with different phases from Garrison et al. (2018). Each box is divided into 25 equal area subvolumes in the $x-y$ plane. In each subvolume $w_{p,\,gg}$ is computed in projection for the fiducial HOD model. We obtain 500 bootstrap resamples by choosing 500 subvolumes with replacement and averaging $w_{p,\,gg}$ for each resample. These bootstrap resamples are used to compute the covariance for $w_{p,\,gg}$. This numerical covariance matrix is inherently noisy and may lead to optimistically biased forecasted parameter constraints. For this reason we also compute the Gaussian covariance for $w_{p,\,gg}$ (e.g. Cooray & Hu 2001; Marian, Smith & Angulo 2015; Krause & Eifler 2017; Singh et al. 2017) and use the diagonal elements of the numerical covariance matrix to normalize the analytic correlation matrix. Thus, our final covariance matrix uses the Gaussian model to compute off-diagonal correlations and the numerical simulations to compute variances and to scale correlations to covariances.

Our forecasts are meant to model DES weak lensing and galaxy clustering with redMaGiC selected galaxies. Consequently, we consider three bins of redshift for our galaxies, $z = 0.15-0.35$, $z = 0.35-0.55$, and $z = 0.55-0.75$, and we assume a survey area of $\Omega = 5000\,\mathrm{deg}^2$. These bins are modelled using AbacusCosmos simulation snapshots at $z = 0.3$, $z = 0.5$, and $z = 0.7$, respectively, which are also assumed as lens redshifts when calculating Σ_{crit}. Mean source redshifts are computed using the source redshift distribution of Rozo, Wu & Schmidt (2011). This source redshift distribution is also used to compute source surface densities in each bin assuming a total source surface density of $\Sigma_{\mathrm{src}} = 10.0\,\mathrm{arcmin}^{-2}$. We assume a shape-noise per galaxy of $\sigma_\gamma = 0.2$.

5 COSMOLOGICAL FORECASTS

5.1 Fiducial scenario

We forecast parameter constraints for our fiducial scenario, a DES-like survey, with the covariance matrix described in Section 4 and derivatives calculated by finite difference from emulator predictions described in Section 3.3. Additionally, we impose a 5 per cent Gaussian prior on the galaxy number density and a 3 per cent prior on A_{lens}. The parameter A_{lens} allows for some amount of scale independent lensing bias. It can be thought of as representing some combination of uncertainty in shear calibration and photometric redshift errors that lead to uncertainty in Σ_{crit}. Our choice of a 3 per cent prior on A_{lens} is loosely motivated by MacCrann et al. (2022) and Myles et al. (2021). Note that we forecast constraints for the natural logarithm of our parameters, except for Q_{cen} and Q_{sat}, which can be zero or negative.

Our fiducial scenario combines $w_{p,\,gg}$ and $\Delta\Sigma$ with information from $0.3\ h^{-1}\,\mathrm{Mpc} < r_p < 30.0 h^{-1}\,\mathrm{Mpc}$ in the $z = 0.35-0.55$ redshift bin. We focus on this single redshift bin for the sake of clarity, chosen because it produces the strongest constraints. In Section 5.4 we examine constraints from our other redshift bins. Results for this fiducial case are shown in Fig. 3. The bottom left block shows our forecast with all cosmological parameters other than Ω_m and σ_8 fixed. The upper right block shows the fiducial constraints on all cosmological parameters (note that these constraints are

[3] fig. 5 of Salcedo et al. (2020b) shows the magnitude of this non-Gaussian contribution, boosting the diagonal elements of the $w_{p,\,gg}$ covariance matrix by a factor of 3 on 1-halo scales.

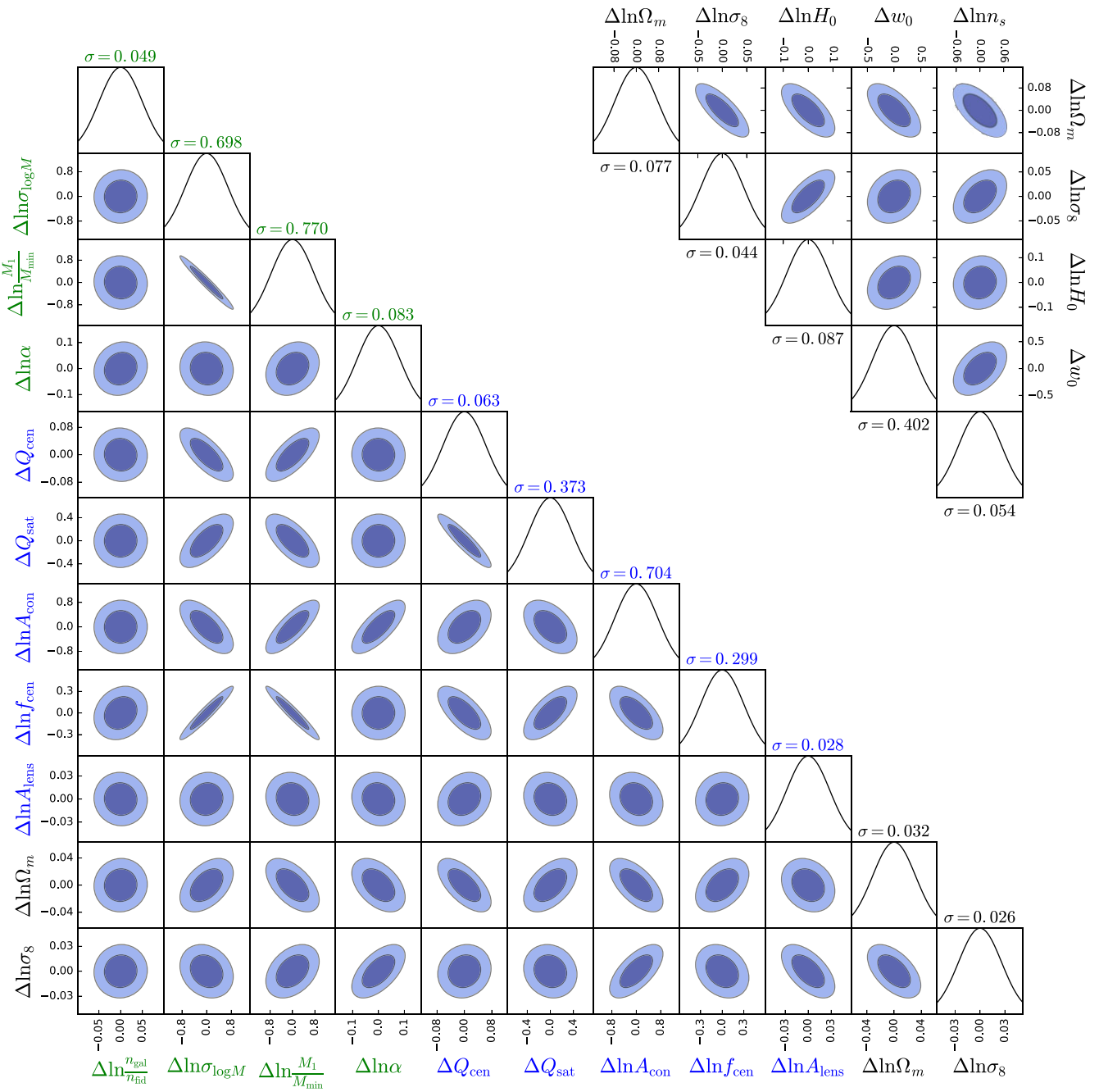

Figure 3. Forecast parameter constraints (68 per cent and 95 per cent contours) for our fiducial scenario, assuming DES-Y6 survey parameters for galaxies between $z = 0.35-0.55$, and using all scales $0.3 < r_p < 30.0\,h^{-1}$ Mpc of $\Delta\Sigma$ and $w_{p,\,gg}$. The bottom block shows constraints on Ω_m and σ_8 and all of our HOD parameters while holding all other cosmological parameters (H_0, w_0, n_s) fixed at their fiducial values. The upper right block shows constraints on all cosmological parameters while marginalizing over all HOD parameters. Fully marginalized errors on each parameter are listed above each PDF panel. Standard HOD parameters are labelled in green, extended HOD parameters in blue, and cosmological parameters in black.

marginalized over all other HOD and nuisance parameters, which have been suppressed for visual clarity). Typically other data, such as CMB anisotropies, the supernova Hubble diagram, and the galaxy power spectrum, provide tight constraints on H_0, w_0, and n_s, so the fixed parameter case is more representative of what DES can achieve on (Ω_m, σ_8) in a multiprobe analysis.

When σ_8 and Ω_m are our only cosmological parameters the best constrained combination of the two is $\sigma_8\Omega_m^{0.438}$, with a 1σ uncertainty of 2.19 per cent after marginalizing over the halo–galaxy connection. Individual marginalized constraints on σ_8 and Ω_m are 2.6 per cent and 3.2 per cent. Our choice to constraint $\sigma_8(z = 0)$ rather than $\sigma_8(z = 0.5)$ affects the $\Omega_m - \sigma_8$ constraint slightly because of the effect of Ω_m on the growth factor, but the effect is smaller than our precision. For example, a 3.0 per cent difference in the value of Ω_m corresponds to a sub-per cent change in the linear growth factor at $z = 0.5$. There are significant degeneracies between σ_8 and HOD or nuisance parameters, particularly $A_{\rm lens}$ and α. In the case of Ω_m, there is a significant degeneracy with $Q_{\rm cen}$, likely due to the large scales of

Table 2. Parameter forecast uncertainties with H_0, w_0, and n_s and fixed, in the $z = 0.5$ bin.

Case	$\Delta\ln A_{\rm lens}$	$\Delta\ln\Omega_m$	$\Delta\ln\sigma_8$	$\Delta\ln S_8$
$\Delta\Sigma$ and $w_{p,gg}$, $A_{\rm lens}$ fixed	–	0.031	0.021	0.012
$\Delta\Sigma$ and $w_{p,gg}$, $A_{\rm lens}$ free, 3 per cent prior	0.028	0.032	0.026	0.022
$\Delta\Sigma$ and $w_{p,gg}$, $A_{\rm lens}$ free, no prior	0.078	0.037	0.047	0.053
$\Delta\Sigma$ and $w_{p,gg}$, No point-mass, $A_{\rm lens}$ fixed	–	0.031	0.021	0.012
$\Delta\Sigma$ and $w_{p,gg}$, No point-mass, $A_{\rm lens}$ free, 3 per cent prior	0.028	0.031	0.026	0.022
$\Delta\Sigma$ and $w_{p,gg}$, No point-mass, $A_{\rm lens}$ free, no prior	0.078	0.036	0.047	0.053

$w_{p,gg}$. Among HOD parameters $\sigma_{\log M}$ and $M_1/M_{\rm min}$ exhibit a strong degeneracy, leading to poor constraints on both parameters. This is unsurprising as both parameters have virtually the same effect on both of our observables (see Fig. 2). Interestingly $f_{\rm cen}$ also exhibits a strong degeneracy with both $\sigma_{\log M}$ and $M_1/M_{\rm min}$, likely due to the way all three parameters affect $w_{p,gg}$. Our two assembly bias parameters, $Q_{\rm cen}$ and $Q_{\rm sat}$, also exhibit a strong degeneracy with each other, likely due to their similar scale dependence at large r_p. Constraints on $Q_{\rm cen}$ are much tighter than constraints on $Q_{\rm sat}$ because it has a much stronger effect on our observables.

When we forecast with all other cosmological parameters free we find constraints of 4.4 per cent and 7.7 per cent on σ_8 and Ω_m, a degradation by roughly a factor of 2. In this case, the best constrained combination of σ_8 and Ω_m is $\sigma_8\Omega_m^{0.444}$ with a forecasted constraint of 2.79 per cent, moderately degraded from the 2.19 per cent constraint with fixed H_0, w_0, and n_s. With DES data alone, much of the ability to break the $\Omega_m - \sigma_8$ degeneracy comes from the shape of $w_{p,gg}$, but the impact of H_0 and n_s on the linear power spectrum is largely degenerate with that of Ω_m. Leaving these parameters free therefore widens the constraints on Ω_m and σ_8 individually but with less impact on their best constrained combination. The value of w_0 has little impact on our observables (Fig. 2), and unsurprisingly we do not forecast a meaningful w_0 constraint. The value of w_0 is somewhat degenerate with σ_8 and Ω_m because σ_8 is defined at $z = 0$ and our observation redshift is $z = 0.5$. If we fix w_0 but leave H_0 and n_s free then the constraint on the best constrained parameter σ_8 and Ω_m combination $\sigma_8\Omega_m^{0.604}$ improves to 2.3 per cent, similar to the case with all three parameters fixed. In contrast, the constraint on Ω_m only improves to 6.0 per cent compared to the 3.2 per cent constraint when H_0, n_s, and w_0 are fixed. We discuss constraints in the $S_8 - \Omega_m$ plane below, for the fiducial scenario and other cases.

5.2 Impact of systematics: $A_{\rm lens}$ and point-mass

Our forecasts include two important sources of systematic uncertainty in $\Delta\Sigma$. As described in Section 4 we modify our lensing covariance to marginalize over an enclosed point-mass. This point-mass marginalization is meant to characterize the impact of baryonic physics on the mass profile within haloes as well as representing small-scale substructure potentially unresolved by our simulations. We also include a multiplicative bias parameter $A_{\rm lens}$ that captures potential scale independent errors in lensing calibration. This may be caused by errors in shear calibration or errors in the measurement of $\Sigma_{\rm crit}$.

To test the sensitivity of constraints to these systematics, we perform a variety of tests and list resulting forecasted constraints on $A_{\rm lens}$, Ω_m, σ_8, and $S_8 = \sigma_8\Omega_m^{0.5}$ in Table 2. In these tests we fix all cosmological parameters besides σ_8 and Ω_m and we marginalize over all HOD parameters. All of these results are for the $z = 0.35{-}0.55$ bin only. Our first series of tests utilizes the full datavector ($\Delta\Sigma$ and $w_{p,gg}$). We see that our constraints on $A_{\rm lens}$ are largely prior dominated; when $A_{\rm lens}$ is free with no prior our datavector only constrains it at the 7.8 per cent level. This significantly degrades our forecast constraint on σ_8, almost doubling the uncertainty from 2.6 per cent to 4.7 per cent, but it has less of an effect on Ω_m.

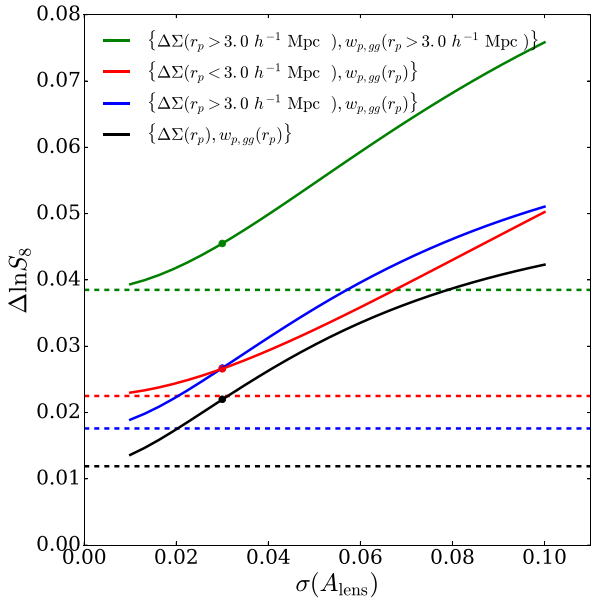

Figure 4. Forecast constraints on $\ln S_8$ as a function of $A_{\rm lens}$ prior in the $z = 0.5$ bin marginalized over all HOD parameters with all other cosmological parameters fixed. The black line shows results from all scales of $\Delta\Sigma$ and $w_{p,gg}$, the red (blue) line shows results from small (large) scales of $\Delta\Sigma$ with all scales of $w_{p,gg}$, and the green line shows the results from large scale of both $\Delta\Sigma$ and $w_{p,gg}$. Points on these lines mark our fiducial forecast assumption of $\sigma(A_{\rm lens}) = 0.03$. Analogously coloured dashed lines show constraints with $A_{\rm lens}$ fixed.

Because the impact of parameters other than $A_{\rm lens}$ is scale-dependent, we might hope that modelling $\Delta\Sigma$ and $w_{p,gg}$ into non-linear scales could break the degeneracy between $A_{\rm lens}$ and cosmology. Table 2 shows that this is only partly the case. If we adopt no prior on $A_{\rm lens}$, then our data vector constrains it to 7.8 per cent and constrains S_8 to 5.3 per cent. This is a huge improvement on linear theory, where $A_{\rm lens}$ and σ_8 are perfectly degenerate. However, with a 3 per cent $A_{\rm lens}$ prior, the posterior uncertainty in $A_{\rm lens}$ is only slightly better at 2.8 per cent. Furthermore, the $A_{\rm lens}$ uncertainty remains a significant limitation, causing the S_8 uncertainty to be 2.2 per cent instead of the much stronger 1.2 per cent that could be achieved if $A_{\rm lens}$ were known perfectly. We further examine the sensitivity of our constraints to our $A_{\rm lens}$ prior in Fig. 4, discussed below.

We next test the robustness of our forecasts to our point-mass marginalization scheme. We repeat each of the previous tests without

Table 3. Parameter forecast uncertainties with H_0, w_0, and n_s fixed in the $z = 0.5$ redshift bin. Also included are constraints on $S_8 = \sigma_8 \Omega_m^{0.5}$. Entries in the first and second columns indicate which scales are *retained* in the $\Delta\Sigma$ and $w_{p,\,gg}$ datavectors, with 'small' indicating 0.3–3.0 h^{-1} Mpc and 'large' indicating 3.0–30.0 h^{-1} Mpc. All cases assume a 3 per cent prior on $A_{\rm lens}$ and marginalization over a point mass contribution to $\Delta\Sigma$.

$\Delta\Sigma$	$w_{p,\,gg}$	$\Delta \ln \frac{n_{\rm gal}}{n_{\rm fid}}$	$\Delta \ln \sigma_{\log M}$	$\Delta \ln \frac{M_1}{M_{\rm min}}$	$\Delta \ln \alpha$	$\Delta Q_{\rm cen}$	$\Delta Q_{\rm sat}$	$\Delta \ln A_{\rm con}$	$\Delta \ln f_{\rm cen}$	$\Delta \ln A_{\rm lens}$	$\Delta \ln \Omega_m$	$\Delta \ln \sigma_8$	$\Delta \ln S_8$
all	all	0.049	0.698	0.334	0.083	0.063	0.373	0.704	0.299	0.028	0.032	0.026	0.022
all	–	0.050	3.353	0.990	0.709	0.275	3.234	5.763	1.095	0.030	0.354	0.233	0.238
–	all	0.050	1.649	0.678	0.162	0.123	0.613	1.108	0.564	0.030	0.061	0.184	0.206
small	all	0.050	1.185	0.521	0.095	0.105	0.472	0.803	0.468	0.030	0.037	0.028	0.027
large	all	0.050	0.858	0.394	0.138	0.066	0.422	1.032	0.350	0.029	0.036	0.034	0.027
all	small	0.050	0.825	0.431	0.139	0.110	0.899	1.172	0.359	0.029	0.065	0.053	0.029
all	large	0.050	1.439	0.594	0.190	0.085	0.522	0.846	0.554	0.029	0.036	0.037	0.030
small	small	0.050	1.558	0.734	0.171	0.250	1.815	1.435	0.638	0.030	0.125	0.079	0.042
large	large	0.050	2.499	1.078	0.628	0.130	0.636	4.756	0.843	0.029	0.040	0.056	0.046

including this modification to the lensing covariance. We see that in this case the point-mass marginalization has very little effect on the final constraints. When $A_{\rm lens}$ is fixed it has a completely negligible effect. When we assume a 3 per cent prior on $A_{\rm lens}$ or assume no prior, the point-mass marginalization has a very small effect on constraints on Ω_m. These results suggest that for our datavector, the small scales of $\Delta\Sigma$ are not the most important regime for constraining Ω_m or σ_8. It may also appear to suggest that the point-mass marginalization is unimportant, but we caution that this depends on the choice of datavector and galaxy sample. Because our assumed lensing covariance is shape-noise dominated, we can imagine a future scenario in which the errors on $\Delta\Sigma$ are substantially improved relative to $w_{p,\,gg}$. Conversely, a sparser lens sample would have larger errors for both $\Delta\Sigma$ and $w_{p,\,gg}$, but the impact on $w_{p,\,gg}$ could be larger. In either scenario, including marginalization over a point-mass would be more important because of the increased relative importance of the small scales of $\Delta\Sigma$. Also, while we are considering point-mass marginalization as a proxy for baryonic physics uncertainties, it is necessary to check that it does in fact remove biases from baryonic effects at the DES statistical precision.

5.3 Relative contributions of scales

Table 3 examines a variety of alternative scenarios in which we omit different elements of the fiducial datavector. In all of these tests we fix all cosmological parameters other than Ω_m and σ_8 and report constraints on $S_8 = \sigma_8 \Omega_m^{0.5}$. We assume our fiducial 3 per cent prior on $A_{\rm lens}$ and 5 per cent prior on $n_{\rm gal}$, and we include the point-mass marginalization term in the lensing covariance matrix. In addition to omitting one of $\Delta\Sigma$ and $w_{p,\,gg}$ entirely, we also try omitting small ($r_p < 3.0\ h^{-1}$ Mpc) and large ($r_p > 3.0\ h^{-1}$ Mpc) scales of either. The choice of 3.0 h^{-1} Mpc roughly corresponds to a division between the linear regime and non-linear regime, and it also splits each observable into equal numbers of data points. The first line of Table 3 ('all all') corresponds exactly to the fiducial scenario shown in Fig. 3. We again focus on the $z = 0.5$ redshift bin for simplicity.

The second line of Table 3 shows a forecast with $\Delta\Sigma$ as the only observable. We see that the precision on all parameters has degraded drastically, except for $n_{\rm gal}$ and $A_{\rm lens}$ which have informative priors. Compared to the fiducial case, the precision on σ_8, Ω_m, S_8 degrades by roughly a factor of 10. This poor performance is unsurprising: without galaxy clustering, galaxy–galaxy lensing in the linear regime has no cosmological constraining power because of degeneracy between b_g and σ_8, and non-linear scale-dependence at DES measurement precision allows only moderate degeneracy breaking.

We next consider the case of $w_{p,\,gg}$ on its own. We again see that all parameter constraints are significantly degraded, although not by as much as in the case of $\Delta\Sigma$ on its own. Constraints on all of our HOD parameters are significantly worse than with the full datavector, but are significantly better than from $\Delta\Sigma$ on its own. This difference is not surprising in the context of Fig. 2, which shows that $w_{p,\,gg}$ is generally more sensitive to the galaxy–halo connection, particularly at small scales. Since many of these HOD parameters are degenerate with each other, these individual improvements in sensitivity synergize with each other to significantly improve overall constraints on the HOD. The large-scale shape of $w_{p,\,gg}$ constrains Ω_m, so the cosmological parameter constraints from $w_{p,\,gg}$ alone are better than those from $\Delta\Sigma$ alone. However, fractional errors in σ_8 and S_8 are still at the 20 per cent level, drastically worse than the fiducial scenario. In linear theory the impact of b_g and σ_8 on $w_{p,\,gg}$ would be fully degenerate. Non-linear scaling provides enough leverage to obtain 20 per cent precision, but σ_8 remains significantly degenerate with HOD parameters. As expected, precise constraints on matter clustering require both $\Delta\Sigma$ and $w_{p,\,gg}$.

The remaining lines of Table 3 show the impact of omitting small- or large-scale measurements from one or both components of the datavector. When we omit the large scales of $\Delta\Sigma$ (line 4, 'small all'), the S_8 constraint degrades to 2.7 per cent from its fiducial value of 2.2 per cent. Both σ_8 and Ω_m are individually degraded. If we retain the large scales of $\Delta\Sigma$ *instead* of the small scales (line 5, 'large all') then the S_8 precision is again 2.7 per cent. The fact that large and small scales of $\Delta\Sigma$ can independently give precise S_8 constraints in concert with $w_{p,\,gg}$ has encouraging implications. Modelling systematics and some measurement systematics are likely to be very different in these two regimes, so comparing inferred parameters will provide a strong test of robustness and a valuable diagnostic of systematics if they are present.

If we retain all scales of $\Delta\Sigma$ but use only the small or large scales of $w_{p,\,gg}$, then S_8 constraints degrade to 2.9 per cent or 3.0 per cent, respectively. HOD constraints are typically much worse if we have only large scales of $w_{p,\,gg}$, so it may seem surprising that S_8 constraints are comparable. However, in the linear regime it is only the overall galaxy bias factor b_g that matters, so large trade-offs among HOD parameters may not have much impact on S_8 precision. Furthermore, the large scales of $w_{p,\,gg}$ provide better Ω_m constraints, so the breaking of $\Omega_m - \sigma_8$ degeneracy is considerably better for the 'all large' scenario than the 'all small' scenario.

The final rows of Table 3 show cases in which we take either large or small scales of both $w_{p,\,gg}$ and $\Delta\Sigma$. The most important takeaway is the large gain in cosmological constraining power from using all scales of $\Delta\Sigma$ and $w_{p,\,gg}$ (first line of Table 3) versus using only scales $r_p > 3.0\,h^{-1}$ Mpc (last line). The improvement on S_8 precision from 4.6 per cent to 2.2 per cent is equivalent to a $(4.6/2.2)^2 \approx 4.4$ increase in survey area. The 'small small' scenario slightly outperforms the 'large large' scenario, with a 4.2 per cent versus 4.6 per cent S_8 precision. However, given the increased modelling complexity of small scales there is no reason to contemplate pursuing this scenario in practice, whereas the 'large large' scenario (in multiple redshift bins) is roughly analogous to the DES key project analyses performed to date.

We summarize and expand upon some of these results in Fig. 4. Curves show the constraint on S_8 marginalized over the HOD with all other cosmological parameters fixed as a function of the prior assumed on $A_{\rm lens}$. Each colour corresponds to a different forecast scenario from Table 3, and analogous dashed lines show the constraint on S_8 when $A_{\rm lens}$ is fixed. The black curve in Fig. 4 shows the relationship between the $A_{\rm lens}$ prior and S_8 when the full datavector is used. We see that if $A_{\rm lens}$ were perfectly known then the best constraint we could achieve with our $z = 0.5$ datavector is about a factor of two narrower than our fiducial scenario, 1.2 per cent versus 2.2 per cent. At large values of $\sigma(A_{\rm lens})$, the curve begins to flatten around $\sigma(A_{\rm lens}) = 0.07$ and asymptote towards a $\sim$5 per cent constraint on S_8. This behaviour is consistent with our results in Table 2; when $A_{\rm lens}$ is completely free our full datavector yields a 7.8 per cent constraint on $A_{\rm lens}$ and a 5.3 per cent constraint on S_8. The red and blue curves correspond to omitting the large and small scales of $\Delta\Sigma$, respectively. Finally the green curve shows results when we omit the small scales of both of our observables. The relative ordering of these curves at a given $\sigma(A_{\rm lens})$ indicates the relative importance of the respective elements of the datavector. Given our fiducial prior on $A_{\rm lens}$, the large and small scales of $\Delta\Sigma$ have similar impact on the constraint on S_8. The large difference between the black and green curves emphasizes the value of the small scales of both observables. If the $\sigma(A_{\rm lens})$ prior could be tightened from 0.03 to 0.01 then the difference between all the scales and large scales analysis would be equivalent a to $(3.93/1.36)^2 \approx 8.35$ times increase in survey area.

5.4 Dependence on redshift

So far we have limited our forecasts to a bin of redshift $z = 0.35{-}0.55$. Since DES redMaGiC galaxies extend from redshift $z = 0.15{-}0.70$, we now consider additional bins at lower and higher redshift. Specifically, we define three bins in redshift, $z = 0.15{-}0.35$, $z = 0.35{-}0.55$, and $z = 0.55{-}0.70$, and we use ABACUS snapshots at $z = 0.3$, $z = 0.5$, and $z = 0.7$, respectively, to compute emulator derivatives. We also compute separate covariance matrices for each bin taking into account the full range in redshift in each bin. Comparing across bins we observe little qualitative difference in derivatives for a given parameter. Quantitatively there is mild evolution, with most parameters having slightly larger effect at low redshift. A more important effect is the evolution of the covariance matrix. For $w_{p,\,gg}$ fractional errors, decrease with increasing redshift because of increasing bin volume. For $\Delta\Sigma$ increasing volume with redshift is counteracted by fewer sources, which increases the shape noise contribution to the covariance and is dependent on the assumed source redshift distribution from Rozo et al. (2011). Fractional errors for $\Delta\Sigma$ improve going from the $z = 0.3$ to $z = 0.5$ redshift bin. However, going from $z = 0.5$ to $z = 0.7$ we find an increase in fractional error because the increase in volume is not able to compensate for the loss in sources.

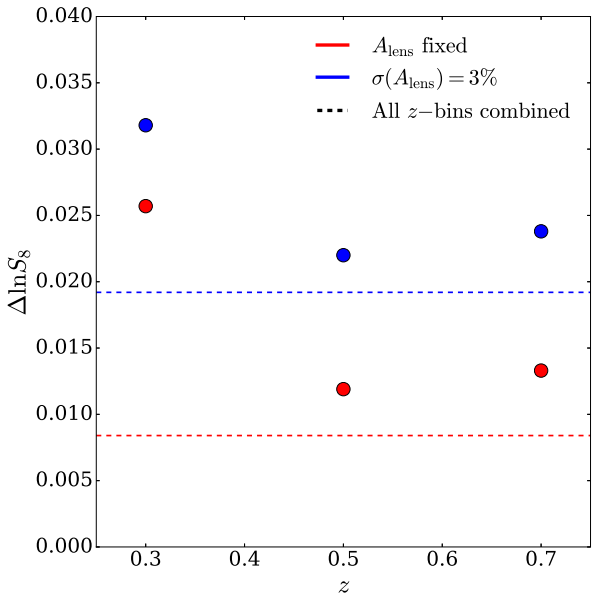

Figure 5. Forecast constraints on $\ln S_8$ as a function of redshift marginalized over all HOD parameters with all other cosmological parameters fixed. Red points show constraints with $A_{\rm lens}$ fixed, while blue points show constraints from including our fiducial 3 per cent prior on $A_{\rm lens}$. Analogously coloured dashed lines show constraints from combining all three of our redshift bins. When combining redshift bins we constrain HOD parameters in each bin separately.

Forecast results in all three redshift bins are shown in Fig. 5. In each bin we forecast constraints on S_8 with our full datavector, $w_{p,\,gg}$ and $\Delta\Sigma$, with all other cosmological parameters fixed. For each bin we perform two separate forecasts in which $A_{\rm lens}$ is fixed (red points) or free with a 3 per cent prior (blue points). Finally we indicate the constraint on S_8 from combining all three bins together with horizontal dashed lines. When combining constraints from multiple redshift bins we allow for different HOD parameters in each redshift bin and we assume redshift bins are independent. When $A_{\rm lens}$ is free we forecast constraints of 3.2 per cent, 2.2 per cent, and 2.4 per cent on S_8 in the $z = 0.3$, $z = 0.5$, and $z = 0.7$ bins, respectively. Fixing $A_{\rm lens}$ improves these constraints to 2.6 per cent, 1.2 per cent, and 1.3 per cent. As expected from our covariance matrices, we see that our constraint improves from $z = 0.3$ to $z = 0.5$. From $z = 0.5$ to $z = 0.7$ the constraint slightly degrades. In this case the precision has improved for $w_{p,\,gg}$ but gotten worse for $\Delta\Sigma$. When all three redshift bins are combined we forecast constraints of 1.9 per cent and 0.8 per cent on S_8 with $A_{\rm lens}$ free and fixed, respectively. Both of these constraints slightly underperform simple quadrature combination of individual constraints.

5.5 Summary

We have forecast cosmological parameter constraints for an analysis of galaxy–galaxy lensing $\Delta\Sigma$ and galaxy clustering $w_{p,\,gg}$ while marginalizing over a flexible HOD model and a scale independent lensing bias parameter $A_{\rm lens}$. Fig. 6 summarizes our main results in the $S_8 - \Omega_m$ plane. The green contours in the left-hand panel show our fiducial scenario combining information from $\Delta\Sigma$ and $w_{p,\,gg}$ measured on scales $0.3\,h^{-1}$ Mpc $< r_p < 30.0\,h^{-1}$ Mpc in a DES-

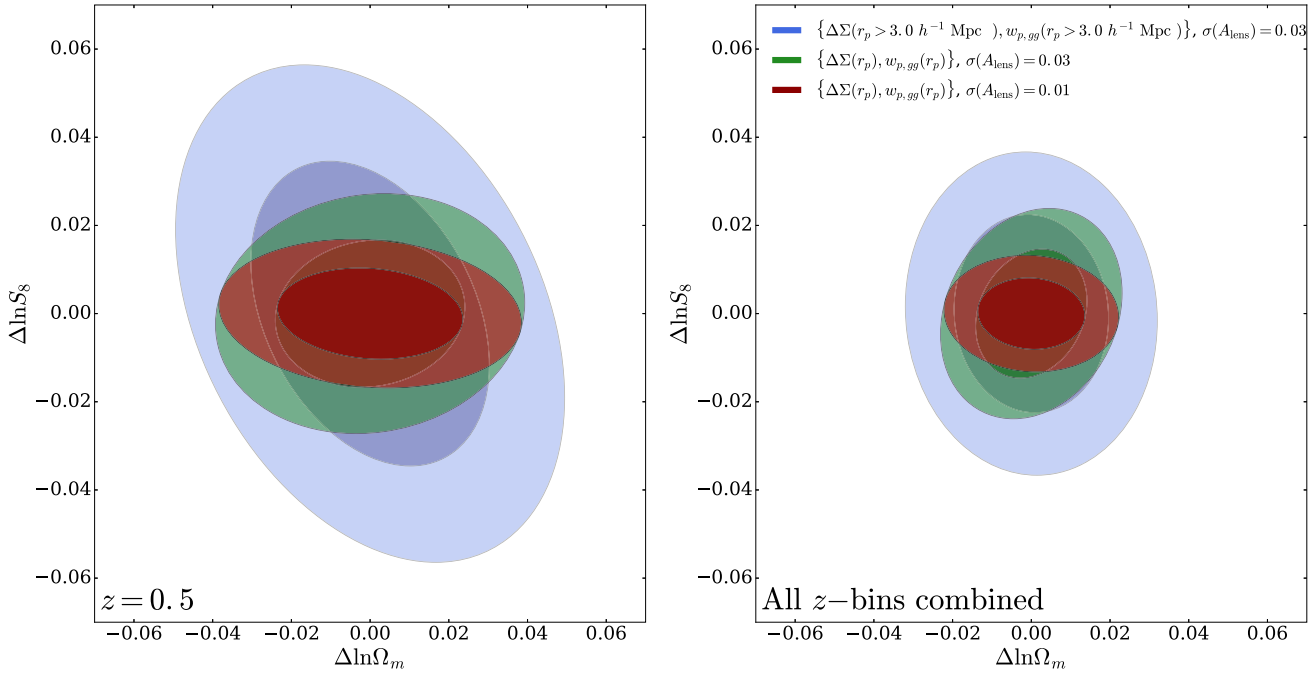

Figure 6. Forecast constraints (68 per cent and 95 per cent contours) on $S_8 = \sigma_8\Omega_m^{0.5}$ and Ω_m with H_0, n_s, and w_0 fixed, summarizing some of our main results. Contours in the left-hand panel show constraints from just the $z = 0.35{-}0.55$ bin, while the right-hand panel shows constraints from combining all three of our redshift bins. Blue contours show constraints when only the large scales of $\Delta\Sigma$ and $w_{p,\,gg}$ are used and a 3 per cent prior on $A_{\rm lens}$ is assumed. Green contours show our fiducial scenario in which all scales of $\Delta\Sigma$ and $w_{p,\,gg}$ are used with a 3 per cent prior on $A_{\rm lens}$. Red contours show constraints from all scales of $\Delta\Sigma$ and $w_{p,\,gg}$ when our prior on $A_{\rm lens}$ is sharpened to 1 per cent.

like survey of galaxies within a bin of redshift $z = 0.35{-}0.55$. For this scenario we forecast 3.2 per cent and 2.2 per cent constraints on Ω_m and S_8. When the 'small' scales ($r_p < 3.0\,h^{-1}$ Mpc) are omitted from such an analysis (blue contours) these constraints are degraded to 4.0 per cent and 4.6 per cent, respectively. This difference in precision on S_8 is equivalent to a ∼4.4-fold increase in survey area, illustrating the stakes of accurate modelling of non-linear scales. If our external prior on $A_{\rm lens}$ is be sharpened to 1 per cent (red contours) then constraints on Ω_m and S_8 sharpen even further to 3.1 per cent and 1.4 per cent, respectively.

In the right-hand panel of Fig. 6 we show results for the same three forecast scenarios when combining all three of our redshift bins spanning $z = 0.15{-}0.70$. When small scales of $\Delta\Sigma$ and $w_{p,\,gg}$ are omitted (blue contours) using all three bins of redshift we forecast a 2.6 per cent and 3.0 per cent constraint on Ω_m and S_8. This constraint on S_8 is an improvement on the 4.6 per cent constraint from the $z = 0.5$ bin, but it is still relatively weak. When the small scales are also included in the datavector we forecast 1.9 per cent constraints on both Ω_m and S_8 (and 2.0 per cent on σ_8). These constraints are an improvement on the 3.2 per cent and 2.2 per cent obtained from the $z = 0.5$ bin, though the S_8 gain is moderate in part because the $A_{\rm lens}$ uncertainty affects all three redshift bins coherently. When the prior on $A_{\rm lens}$ is reduced to 1 per cent these constraints improve to 1.8 per cent on Ω_m, 1.4 per cent on σ_8, and 1.1 per cent constraint on S_8. This result shows the impressive gains that are attainable if future analyses can include small-scale information from galaxy–galaxy lensing and clustering while controlling the uncertainty in lensing calibration over a broad range in redshift $z = 0.15{-}0.70$. Our forecasts show that if those conditions are met the degeneracy between Ω_m and σ_8 can be broken to yield per cent-level constraints on the amplitude of matter clustering.

Fig. 7 presents a different summary form of our results, with an emphasis on the information content of smaller scales. Here we have

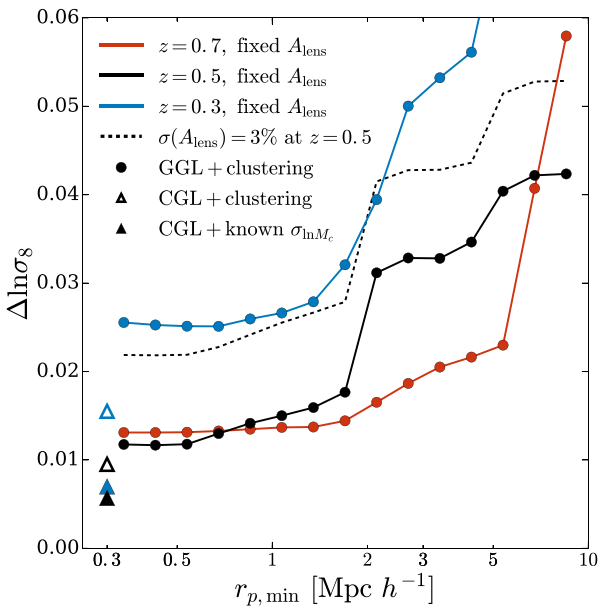

Figure 7. Forecast constraints on $\ln\sigma_8$ as a function of minimum scale of $\Delta\Sigma$ and $w_{p,\,gg}$. The constraint on $\ln\sigma_8$ is marginalized over all HOD parameters with all other cosmological parameters fixed. The black solid line shows the case for the fiducial bin at $z = 0.5$ with $A_{\rm lens}$ fixed, while blue and red lines show results from the $z = 0.3$ and $z = 0.7$ bins. The dashed black line shows the case for the fiducial bin at $z = 0.5$ with $A_{\rm lens}$ included with our fiducial 3 per cent prior. For the sake of comparison analogously coloured triangles show constraints from the cluster weak-lensing $\Delta\Sigma$, $w_{p,\,cg}$, and $w_{p,\,gg}$ datavector of Salcedo et al. (2020b) using all scales of $0.3 < r_p < 30.0\,h^{-1}$ Mpc. Filled in triangles show constraints for the case of fixed scatter in the cluster mass–observable relation $\sigma_{\ln M_c}$, while empty triangles show the case of free $\sigma_{\ln M_c}$.

forecast constraints on σ_8 with fixed values of the other cosmological parameters including Ω_m; in a given redshift bin, fractional errors on σ_8 at fixed Ω_m are similar to the errors on S_8 with free Ω_m. Filled circles and connecting solid curves show forecast constraints for the three redshift bins with fixed $A_{\rm lens}$, as a function of the minimum scale included in both $\Delta\Sigma$ and $w_{p,\,gg}$ (with $r_{p,\rm max}$=30.0 h^{-1} Mpc in all cases). At $z = 0.5$, the precision on σ_8 degrades moderately as $r_{p,\,\rm min}$ increases from 0.3 h^{-1} Mpc to 1.8 h^{-1} Mpc, then degrades sharply as $r_{p,\,\rm min}$ crosses 2.0 h^{-1} Mpc. For $z = 0.7$, the precision with small $r_{p,\,\rm min}$ is similar to $z = 0.5$, and it degrades more slowly with increasing $r_{p,\,\rm min}$ until jumping sharply at $r_{p,\rm min}$=8.0 h^{-1} Mpc. For $z = 0.3$, the precision is lower as explained previously, and it is nearly constant for $r_{p,\rm min} \leq 1.0\,h^{-1}$ Mpc. The black dashed curve shows the forecast at $z = 0.5$ with a 3 per cent prior on $A_{\rm lens}$. The $A_{\rm lens}$ uncertainty significantly degrades the σ_8 precision, as shown previously in Table 2, but the loss is smaller than one would expect from a naive quadrature combination of the $A_{\rm lens}$ and σ_8 uncertainties, even though both parameters have the same effect on $\Delta\Sigma$ in linear theory. Determining σ_8 with a precision tighter than the $A_{\rm lens}$ prior is a benefit of working into the non-linear regime, where the impact of σ_8 is scale-dependent.

Open triangles show the σ_8 precision forecasts from Salcedo et al. (2020b) for a combination of three observables: cluster weak lensing profiles $\Delta\Sigma_c(r_p)$, the projected cluster–galaxy cross-correlation function $w_{p,\,cg}(r_p)$, and the projected galaxy–galaxy correlation function $w_{p,\,gg}(r_p)$. These forecasts are computed in the $z = 0.15{-}0.35$ and $z = 0.35{-}0.55$ redshift bins assuming DES-like cluster samples and weak lensing and clustering measurements, with fixed $A_{\rm lens}$. We see that this three-observable combination can attain a σ_8 precision comparable to that of GGL + clustering at $z = 0.5$ and better at $z = 0.3$. Salcedo et al. (2020b) do not compute a forecast for $z = 0.7$. Although some systematics would be in common between these two analyses such as uncertainties in shear calibration and source photometric redshifts, many systematics would be different. It is encouraging that clusters and GGL offer parallel routes to high-precision constraints on matter clustering from DES. The three-observable combination considered by Salcedo et al. (2020b) constrains the scatter $\sigma_{\ln M_c}$ between true cluster mass and an observable mass proxy such as richness, which is the most important nuisance parameter that affects cosmological constraints from cluster weak lensing. Filled triangles show the still tighter constraints that could be derived from cluster $\Delta\Sigma_c$ alone if $\sigma_{\ln M_c}$ were known independently. Wu et al. (2021) discuss cluster weak lensing constraints and the trade-off with $\sigma_{\ln M_c}$ and survey parameters in greater detail.

6 CONCLUSIONS

We have investigated potential cosmological constraints from a combination of galaxy–galaxy lensing $\Delta\Sigma$ and galaxy clustering $w_{p,\,gg}$ measured using redMaGiC selected galaxies with the precision expected in the final (Y6) data release of DES. We have computed observables using simulations from the AbacusCosmos suite (Garrison et al. 2018) of *N*-body simulations and populating haloes with mock galaxies using a flexible HOD parametrization that includes central and satellite galaxy assembly bias. Using these observables we have constructed Gaussian process emulators (Wibking et al. 2020) of $w_{p,\,gg}$ and $\Delta\Sigma$, which accurately model each observable over a wide range of scales 0.3–30.0 h^{-1} Mpc and a large space of HOD and cosmological parameters. We have also included in our analysis the effects of biased lensing calibration, represented by the parameter $A_{\rm lens}$. We assume a fiducial HOD that is meant to describe the clustering of redMaGiC selected galaxies in DES; these values are listed in Table 1. To compute covariance matrices we have used a mixture of analytic and numerical methods described in Section 4. To represent potential measurements and modelling systematics, we have included a parameter $A_{\rm lens}$ that multiplies all scales of $\Delta\Sigma$ by a common factor, and we have modified the weak lensing covariance matrix to analytically marginalize over a point mass contribution to $\Delta\Sigma$. These parameters can represent effects such as shear calibration bias, photo-z bias, or baryonic modification of halo density profiles on small scales.

With a 3 per cent prior on $A_{\rm lens}$, we forecast precision of 1.9 per cent and 2.0 per cent on Ω_m and σ_8, respectively, from the combination of all three redshift bins, with fixed values of H_0, n_s, and w_0 and separate marginalization over all HOD parameters in each redshift bin. The precision on S_8 is 1.9 per cent. If the prior on $A_{\rm lens}$ is sharpened to 1 per cent, then the S_8 constraint tightens to 1.1 per cent. Our results demonstrate the great promise of modelling GGL and galaxy clustering into the non-linear regime using HOD and *N*-body + emulator methods. If we restrict our datavectors to scales $r_p \geq 3.0\,h^{-1}$ Mpc then the S_8 precision degrades by a factor of 1.6, equivalent to a factor of 2.5 in survey area. For the 1 per cent $A_{\rm lens}$ prior the benefit of small scales is even larger, a factor of 2.8 in S_8 precision (a factor of 7.7 in equivalent survey area). For the $z = 0.5$ redshift bin, Sections 5.1–5.3 examine the correlations between HOD and cosmological parameters, the impact of different systematics assumptions, and the contribution of different scales of the two observables (Figs 2–4 and Tables 2 and 3). In our forecasts, point-mass marginalization does not noticeably degrade cosmological parameter precision, but uncertainty $\geq$ 1 per cent in $A_{\rm lens}$ does.

The recent DES-Y3 3 × 2pt. cosmological analysis (DES Collaboration 2021) uses only large-scale lensing and clustering data and obtains 9.3 per cent, 6.1 per cent, and 2.2 per cent constraints on Ω_m, σ_8, and S_8. Comparison to our forecasts is difficult because this analysis includes cosmic shear, uses a magnitude-limited sample instead of redMaGiC, uses lower depth (Y3 versus Y6) DES data, and includes nuisance parameters we have not considered here (such as intrinsic alignments). Closer to our scenarios, Pandey et al. (2021) analysed DES-Y3 redMaGiC lensing and clustering in the linear regime, obtaining 10.7 per cent and 4.2 per cent constraints on Ω_m and S_8. They caution that their S_8 results are likely biased by an unknown systematic causing internal inconsistency between redMaGiC lensing and clustering. We have implicitly assumed that this challenge can be overcome by the time of the final DES analyses and that remaining systematics can be adequately encapsulated by our $A_{\rm lens}$ parameter even if they arise from multiple contributing factors.

Our emulator already appears accurate enough for the expected precision of final DES redMaGiC data (see Fig. 1), though further testing and training on still larger simulation suites is desirable. We expect that our methods can be readily adapted to magnitude-limited samples, which should allow more precise $\Delta\Sigma$ measurements that require more careful treatment of photo-z errors. Fortunately, in addition to affording high statistical precision, analyses that extend to non-linear scales provide rich opportunities for internal consistency checks and systematics tests, through distinctive scale dependence and comparison among galaxy samples that have different HODs but should yield consistent cosmological parameters. For our $z = 0.5$ forecast with all scales used in $w_{p,\,gg}$, we find essentially equal cosmological precision using scales $r_p > 3\,h^{-1}$ Mpc and $r_p < 3\,h^{-1}$ Mpc in $\Delta\Sigma$, allowing a strong consistency check between regimes where many systematics are very different. If there is a 5–10 per cent

discrepancy between low redshift matter clustering and CMB-normalized ΛCDM predictions, as suggested by some but not all recent weak lensing studies, then final DES analyses will demonstrate the discrepancy at high precision and allow initial explorations of its redshift and scale dependence. Alternatively, if early universe fluctuations and low redshift matter clustering are consistent at the 1 per cent level, then maximally exploiting the potential of Stage III weak lensing surveys will demonstrate impressive success of standard cosmology and prepare the way for Stage IV dark energy experiments that are underway or beginning soon.

ACKNOWLEDGEMENTS

We thank the anonymous referee for their helpful comments. We thank the creators of the Abacus Cosmos simulation suite for producing this powerful public resource, with special thanks to Lehman Garrison and Daniel Eisenstein for useful conversations. We thank Ami Choi, Jack Elvin-Poole, Niall MacCrann, Michael Troxel, and Ashley Ross for helpful discussions of Dark Energy Survey weak lensing and galaxy clustering. This work was supported in part by National Science Foundation grant AST-2009735. ANS was supported by a Department of Energy Computational Science Graduate Fellowship. This material is based upon work supported by the U.S. Department of Energy, Office of Science, Office of Advanced Scientific Computing Research, Department of Energy Computational Science Graduate Fellowship under Award Number DE-FG02-97ER25308. DW acknowledges the hospitality of the Institute for Advanced Study and the support of the W.M. Keck Foundation and the Hendricks Foundations during phases of this work. HW is supported by the Department of Energy Grant DE-SC0021916. Simulations were analysed in part on computational resources of the Ohio Supercomputer Center (Ohio Supercomputer Center 1987), with resources supported in part by the Center for Cosmology and AstroParticle Physics at the Ohio State University. We gratefully acknowledge the use of the MATPLOTLIB software package (Hunter 2007) and the GNU Scientific library (Galassi et al. 2009). This research has made use of the SAO/NASA Astrophysics Data System.

This report was prepared as an account of work sponsored by an agency of the United States Government. Neither the United State Government nor any agency thereof, nor any of their employees, makes any warranty, express or implied, or assumes any legal liability or responsibility for the accuracy, completeness, or usefulness of any information, apparatus, product, or process disclosed, or represents that its use would not infringe on privately owned rights. Reference herein to any specific commercial product, process, or service by trade name, trademark, manufacturer or otherwise does not necessarily constitute or imply its endorsement, recommendation, or favouring by the United States Government or any agency thereof. The views and opinions of authors expressed herein do not necessarily state or relect those of the United State Government or any agency thereof.

DATA AVAILABILITY

No new data were generated or analysed in support of this research.

REFERENCES

Amon A. et al., 2021, preprint (arXiv:2105.13543)
Anderson L. et al., 2014, MNRAS, 441, 24
Artale M. C., Zehavi I., Contreras S., Norberg P., 2018, MNRAS, 480, 3978
Behroozi P. S., Wechsler R. H., Wu H.-Y., 2013, ApJ, 762, 109
Benson A. J., Cole S., Frenk C. S., Baugh C. M., Lacey C. G., 2000, MNRAS, 311, 793
Berlind A. A., Weinberg D. H., 2002, ApJ, 575, 587
Bose S., Eisenstein D. J., Hernquist L., Pillepich A., Nelson D., Marinacci F., Springel V., Vogelsberger M., 2019, MNRAS, 490, 5693
Bryan G. L., Norman M. L., 1998, ApJ, 495, 80
Cacciato M., van den Bosch F. C., More S., Li R., Mo H. J., Yang X., 2009, MNRAS, 394, 929
Cacciato M., Lahav O., van den Bosch F. C., Hoekstra H., Dekel A., 2012, MNRAS, 426, 566
Cacciato M., van den Bosch F. C., More S., Mo H., Yang X., 2013, MNRAS, 430, 767
Conroy C., Wechsler R. H., Kravtsov A. V., 2006, ApJ, 647, 201
Contreras S., Zehavi I., Padilla N., Baugh C. M., Jiménez E., Lacerna I., 2019, MNRAS, 484, 1133
Cooray A., 2006, MNRAS, 365, 842
Cooray A., Hu W., 2001, ApJ, 554, 56
Cooray A., Sheth R., 2002, Phys. Rep., 372, 1
Correa C. A., Wyithe J. S. B., Schaye J., Duffy A. R., 2015, MNRAS, 452, 1217
Coupon J. et al., 2012, A&A, 542, A5
Croton D. J., Gao L., White S. D. M., 2007, MNRAS, 374, 1303
DES Collaboration, 2021, preprint (arXiv:2105.13549)
Eisenstein D. J., Hu W., 1998, ApJ, 496, 605
Faltenbacher A., White S. D. M., 2010, ApJ, 708, 469
Frieman J. A., Turner M. S., Huterer D., 2008, ARA&A, 46, 385
Galassi M., Davies J., Theiler J., Gough B., Jungman G., Alken P., Booth M., Rossi F., 2009, GNU Scientific Library Reference Manual. 3 edn
Gao L., White S. D. M., 2007, MNRAS, 377, L5
Gao L., Springel V., White S. D. M., 2005, MNRAS, 363, L66
Garrison L. H., Eisenstein D. J., Ferrer D., Tinker J. L., Pinto P. A., Weinberg D. H., 2018, ApJS, 236, 43
Guo H. et al., 2014, MNRAS, 441, 2398
Harker G., Cole S., Helly J., Frenk C., Jenkins A., 2006, MNRAS, 367, 1039
Heitmann K., Higdon D., White M., Habib S., Williams B. J., Lawrence E., Wagner C., 2009, ApJ, 705, 156
Hikage C. et al., 2019, PASJ, 71, 43
Hildebrandt H. et al., 2017, MNRAS, 465, 1454
Hunter J. D., 2007, Comput. Sci. Eng., 9, 90
Jee M. J., Tyson J. A., Hilbert S., Schneider M. D., Schmidt S., Wittman D., 2016, ApJ, 824, 77
Jing Y. P., Mo H. J., Börner G., 1998, ApJ, 494, 1
Jing Y. P., Suto Y., Mo H. J., 2007, ApJ, 657, 664
Johnson J. W., Maller A. H., Berlind A. A., Sinha M., Holley-Bockelmann J. K., 2019, MNRAS, 486, 1156
Joudaki S. et al., 2018, MNRAS, 474, 4894
Krause E., Eifler T., 2017, MNRAS, 470, 2100
Krolewski A., Ferraro S., White M., 2021, J. Cosmol. Astropart. Phys., 2021, 028
Lange J. U., van den Bosch F. C., Zentner A. R., Wang K., Villarreal A. S., 2019, MNRAS, 482, 4824
Lange J. U., Leauthaud A., Singh S., Guo H., Zhou R., Smith T. L., Cyr-Racine F.-Y., 2021, MNRAS, 502, 2074
Leauthaud A., Tinker J., Behroozi P. S., Busha M. T., Wechsler R. H., 2011, ApJ, 738, 45
Leauthaud A. et al., 2012, ApJ, 744, 159
Leauthaud A. et al., 2017, MNRAS, 467, 3024
Li Y., Mo H. J., Gao L., 2008, MNRAS, 389, 1419
MacCrann N., Blazek J., Jain B., Krause E., 2020, MNRAS, 491, 5498
MacCrann N. et al., 2022, MNRAS, 509, 3371
Ma C.-P., Fry J. N., 2000, ApJ, 543, 503
Mandelbaum R., Seljak U., Kauffmann G., Hirata C. M., Brinkmann J., 2006, MNRAS, 368, 715
Mandelbaum R., Slosar A., Baldauf T., Seljak U., Hirata C. M., Nakajima R., Reyes R., Smith R. E., 2013, MNRAS, 432, 1544
Mansfield P., Kravtsov A. V., 2020, MNRAS, 493, 4763
Mao Y.-Y., Zentner A. R., Wechsler R. H., 2018, MNRAS, 474, 5143

Marian L., Smith R. E., Angulo R. E., 2015, MNRAS, 451, 1418
McCarthy K. S., Zheng Z., Guo H., 2019, MNRAS, 487, 2424
McEwen J. E., Weinberg D. H., 2018, MNRAS, 477, 4348
More S., van den Bosch F. C., Cacciato M., More A., Mo H., Yang X., 2013, MNRAS, 430, 747
More S., Miyatake H., Mandelbaum R., Takada M., Spergel D. N., Brownstein J. R., Schneider D. P., 2015, ApJ, 806, 2
Myles J. et al., 2021, MNRAS, 505, 4249
Navarro J. F., Frenk C. S., White S. D. M., 1997, ApJ, 490, 493
Ohio Supercomputer Center, 1987, Ohio Supercomputer Center. Available at http://osc.edu/ark:/19495/f5s1ph73
Pandey S. et al., 2021, preprint (arXiv:2105.13545)
Peacock J. A., Smith R. E., 2000, MNRAS, 318, 1144
Planck Collaboration XIII, 2016, A&A, 594, A13
Porredon A. et al., 2021, Phys. Rev. D, 103, 043503
Prat J. et al., 2021, preprint (arXiv:2105.13541)
Rozo E. et al., 2016, MNRAS, 461, 1431
Rozo E., Wu H.-Y., Schmidt F., 2011, ApJ, 735, 118
Salcedo A. N., Maller A. H., Berlind A. A., Sinha M., McBride C. K., Behroozi P. S., Wechsler R. H., Weinberg D. H., 2018, MNRAS, 475, 4411
Salcedo A. N. et al., 2020a, preprint (arXiv:2010.04176)
Salcedo A. N., Wibking B. D., Weinberg D. H., Wu H.-Y., Ferrer D., Eisenstein D., Pinto P., 2020b, MNRAS, 491, 3061
Sato-Polito G., Montero-Dorta A. D., Abramo L. R., Prada F., Klypin A., 2019, MNRAS, 487, 1570
Scoccimarro R., Sheth R. K., Hui L., Jain B., 2001, ApJ, 546, 20
Secco L. F. et al., 2021, preprint (arXiv:2105.13544)
Seljak U., 2000, MNRAS, 318, 203
Sheth R. K., Tormen G., 2004, MNRAS, 350, 1385
Singh S., Mandelbaum R., Seljak U., Slosar A., Vazquez Gonzalez J., 2017, MNRAS, 471, 3827
Singh S., Mandelbaum R., Seljak U., Rodríguez-Torres S., Slosar A., 2020, MNRAS, 491, 51
Sinha M., Garrison L., 2017, Astrophysics Source Code Library, record ascl:1703.003
The Dark Energy Survey Collaboration, 2005, preprint (arXiv:astro–ph/0510346)
Tinker J., Kravtsov A. V., Klypin A., Abazajian K., Warren M., Yepes G., Gottlöber S., Holz D. E., 2008, ApJ, 688, 709
Tinker J. L., Robertson B. E., Kravtsov A. V., Klypin A., Warren M. S., Yepes G., Gottlöber S., 2010, ApJ, 724, 878
Tucci B., Montero-Dorta A. D., Abramo L. R., Sato-Polito G., Artale M. C., 2021, MNRAS, 500, 2777
Vale A., Ostriker J. P., 2006, MNRAS, 371, 1173
van den Bosch F. C., Yang X., Mo H. J., 2003, MNRAS, 340, 771
Wang Z. et al., 2019, ApJ, 879, 71
Wang H. Y., Mo H. J., Jing Y. P., 2007, MNRAS, 375, 633
Wechsler R. H., Zentner A. R., Bullock J. S., Kravtsov A. V., Allgood B., 2006, ApJ, 652, 71
Weinberg D. H., Mortonson M. J., Eisenstein D. J., Hirata C., Riess A. G., Rozo E., 2013, Phys. Rep., 530, 87
Wibking B. D. et al., 2019, MNRAS, 484, 989
Wibking B. D., Weinberg D. H., Salcedo A. N., Wu H.-Y., Singh S., Rodríguez-Torres S., Garrison L. H., Eisenstein D. J., 2020, MNRAS, 492, 2872
Wu H.-Y., Weinberg D. H., Salcedo A. N., Wibking B. D., Zu Y., 2019, MNRAS, 490, 2606
Wu H.-Y., Weinberg D. H., Salcedo A. N., Wibking B. D., 2021, ApJ, 910, 28
Xu X., Zheng Z., 2018, MNRAS, 479, 1579
Xu X., Zehavi I., Contreras S., 2021, MNRAS, 502, 3242
Yang X., Mo H. J., van den Bosch F. C., 2003, MNRAS, 339, 1057
Yoo J., Seljak U., 2012, Phys. Rev. D, 86, 083504
Yoo J., Tinker J. L., Weinberg D. H., Zheng Z., Katz N., Davé R., 2006, ApJ, 652, 26
Zehavi I. et al., 2011, ApJ, 736, 59
Zehavi I., Contreras S., Padilla N., Smith N. J., Baugh C. M., Norberg P., 2018, ApJ, 853, 84
Zheng Z., Weinberg D. H., 2007, ApJ, 659, 1
Zheng Z. et al., 2005, ApJ, 633, 791
Zheng Z., Zehavi I., Eisenstein D. J., Weinberg D. H., Jing Y. P., 2009, ApJ, 707, 554
Zu Y., Mandelbaum R., 2015, MNRAS, 454, 1161
Zu Y., Zheng Z., Zhu G., Jing Y. P., 2008, ApJ, 686, 41

This paper has been typeset from a TEX/LATEX file prepared by the author.